Ore Geology Reviews 150 (2022) 105129

Contents lists available at ScienceDirect

Ore Geology Reviews

journal homepage: www.elsevier.com/locate/oregeorev

Geology and geochemistry of the high-grade Zankan magnetite ore, Western Kunlun Mountains, NW China

Zhiquan Li [a,b], Yongzhang Zhou [a,*], Pengpeng Yu [a,*], Lianchang Zhang [c], Wei Wei [d], Yuhao Li [b], Kurt O. Konhauser [b], Leslie J. Robbins [e]

[a] Guangdong Provincial Key Lab of Geological Process and Mineral Resources Survey, School of Earth Sciences and Geological Engineering, Sun Yat-sen University, Guangzhou 510275, China
[b] Department of Earth & Atmospheric Sciences, University of Alberta, Edmonton, Alberta T6G 2E3, Canada
[c] Key Laboratory of Mineral Resources, Institute of Geology and Geophysics, Chinese Academy of Sciences, Beijing 100029, China
[d] School of Earth Sciences, China University of Geosciences, Wuhan 430074, China
[e] Department of Geology, University of Regina, Regina, Saskatchewan S4S 0A2, Canada

ARTICLE INFO

Keywords:
Iron formation
High-grade magnetite ores
Dacite-porphyry
Silica leaching
The Zankan iron deposit
Western Kunlun Mountains

ABSTRACT

Over the past decade, several magnetite-rich iron deposits have been discovered in the Taxkorgan region of the western Kunlun Mountains of northwestern China. These include the Zankan, Jiertieke, Laobing, Yelike, and Taaxi iron deposits. Prospective iron ore reserves are estimated at over 1 billion tons, with an average magnetite grade of 28% (Feng et al., 2018). The largest of the deposits, the Zankan Iron Deposit (ZID), is estimated to contain 628 million tons of iron ore, with at least 10% of the ores being high-grade (TFe > 50 wt%). However, the geological processes by which the high-grade ores in the ZID were formed remains poorly constrained. In this study, we combine whole rock and ore geochemistry data, oxygen and sulfur stable isotopes, and uranium-lead and hafnium isotopes from zircons to elucidate the plausible mechanisms underpinning the formation of the ZID ores. Based on mineralogy, we define two ore types. Type 1 is essentially comprised of quartz and magnetite, interlayered with schist, and it retains the sedimentary fabrics of the precursor iron-rich sediments which were an iron formation (IF). Type 2 formed by the intrusion of a dacite-porphyry into the IF which led to magnetite remobilization and recrystallization as manifest in magnetite-ferro actinolite veining. Rare earth element (REE) characteristics of the high-grade ores differs from those of the precursor IF, with chondrite normalized REE patterns showing enrichment of LREE and significant negative europium anomalies close to those of the dacite-porphyry. The oxygen and sulfur isotopic composition of magnetite and pyrite in the high-grade ores suggests a further meteoric influence on the ZID with silica enrichment driven by leaching of the precursor IF from elsewhere in the sequence. Circulation of the ore forming fluid is attributable to the development of faults and fracture zones that resulted from the intrusion of the dacite-porphyry. Laser ablation uranium-lead analyses of zircons from the dacite-porphyry yield two groups with ages of 551.25 ± 3.32 Ma and 497.82 ± 3.81 Ma, representing captured detrital zircons and the intrusive age of dacite porphyry, respectively. Given the intimate geological relationship between the dacite-porphyry and T2 ore, we suggest that the high-grade ores are formed after 497.82 Ma. Collectively our field observations and geochemical data reveal the detailed alteration processes that led to the development of the high-grade iron ores in the ZID, identifying distinctive features that may help to guide future exploration for additional high-grade ore deposits in the Taxkorgan region.

1. Introduction

Iron formations (IFs) are iron-rich (15–40 wt% Fe) and siliceous (40–60 wt% SiO_2) chemical sedimentary rocks that precipitated from seawater throughout Earth's history (Konhauser et al., 2017), with the majority of high-grade iron ore deposits mined today being hosted by IFs (Beukes et al., 2008). As such, it is critical to understand the mechanisms that led to the genesis of high-grade iron ores from the precursor IFs. Previous studies have defined IF hosted high-grade ores as having TFe > 60 wt%. This definition is primarily based on hematite-rich iron ore

* Corresponding authors.
E-mail addresses: zhouyz@mail.sysu.edu.cn (Y. Zhou), yupengp@mail2.sysu.edu.cn (P. Yu).

https://doi.org/10.1016/j.oregeorev.2022.105129
Received 26 May 2022; Received in revised form 8 September 2022; Accepted 26 September 2022
Available online 26 September 2022

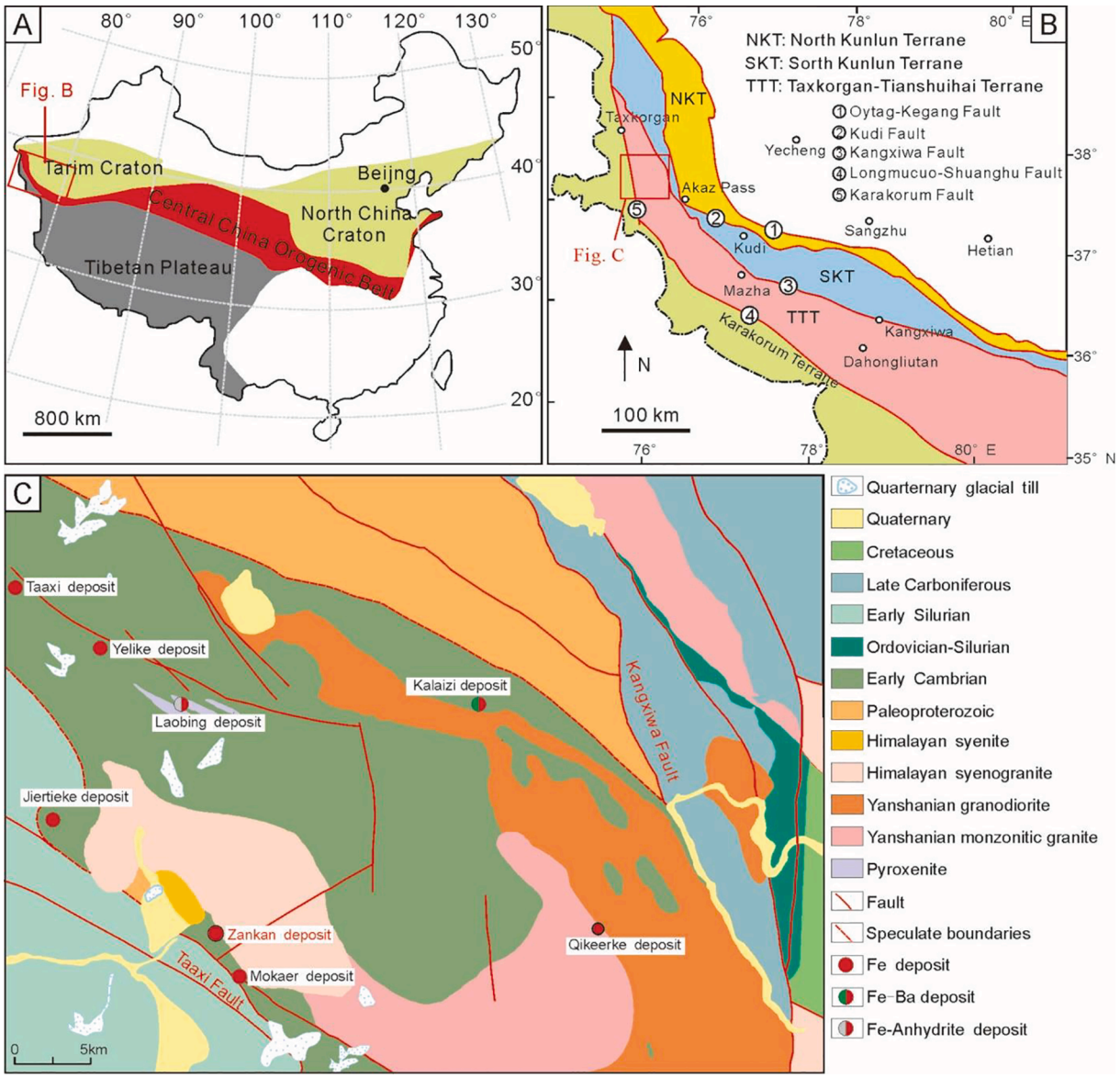

Fig. 1. (A) The tectonic subdivisions of China, showing the location of the Western Kunlun Orogenic Belt. (B) Tectonic subdivisions of the Western Kunlun Orogenic Belt, highlighting the location of the Taxkorgan region. (C) Geological map and distribution of iron deposits in the Taxkorgan region. (A) and (B) modified from Zhou et al. (2017) and (C) after Zhang et al. (2016).

deposits from Australia, South Africa and Brazil (Hagemann et al., 2008; Beukes et al., 2008; Thorne et al., 2009). However, IF related ore deposits in China are mainly composed of magnetite-dominated IFs with an average of 30 wt% Fe. As a result, in China high-grade magnetite ores are defined as having TFe >50 wt% (see Chinese national standard: DZ/T 0200-2002), in part this is because iron ores that are sedimentary in origin in China are typically of a lower grade when compared to other major iron mining areas (Li et al., 2015). It is generally believed that the genesis of high-grade iron ores hosted in IF can be ascribed to one of three models: (1) syngenetic models where synsedimentary or diagenetic structures, such as extensional faults, boudinage controlled lithofacies variations, or diagenetic modifications, led to chert-free IF (Findlay, 1994; Lascelles, 2007); (2) supergene and associated metamorphic models that depend on ancient or recent meteoric waters leaching gangue minerals through high-permeability zones or analogous structures (Morris and Wolff, 1985; Powell et al., 1999; Ramanaidou, 2009); (3) hypogene-supergene models that propose a multistage upgrading processes of IF (e.g., Barley et al., 1999; Taylor et al., 2001; Thorne et al., 2004), in which alteration is mainly driven by high temperature hydrothermal fluids (>150 °C, and possibly > 250 °C) that interact with the original IF units and result in iron oxide mineralization and the removal of silica (Taylor et al., 2001; Dalstra and Rosière, 2008; Zhang et al., 2014; Shen and Song, 2015). Each of these models relies on the presence of more permeable structures (e.g., faults, fracture zones) which allow transportation of the ore forming fluid (e.g., hydrothermal, meteoric, or metamorphic fluids) and leads to the precursor IFs being upgraded to orebodies.

The Western Kunlun Orogenic Belt (WKOB) extends from the northern margin of the Tibetan Plateau to the southern margin of the Tarim Basin, representing a key tectonic junction between the Pan-Asia and Tethyan tectonic domains. Several large magnetite-rich iron deposits (e.g., Zankan, Jiertieke, Yelike, Laobing, and Taaxi) have been discovered in the Taxkorgan region of the WKOB and are present as an iron ore belt in this region (Fig. 1). The largest of these deposits, the Zankan iron deposit (ZID), has reported iron mineral resources of > 628 $\times 10^6$ tons, with an exploration potential of > 942 $\times 10^6$ tons of iron ores. To date, reserves of high-grade Fe ore (i.e., TFe > 50 wt%) account for about 10% of the measured mineral resources of the entire deposit

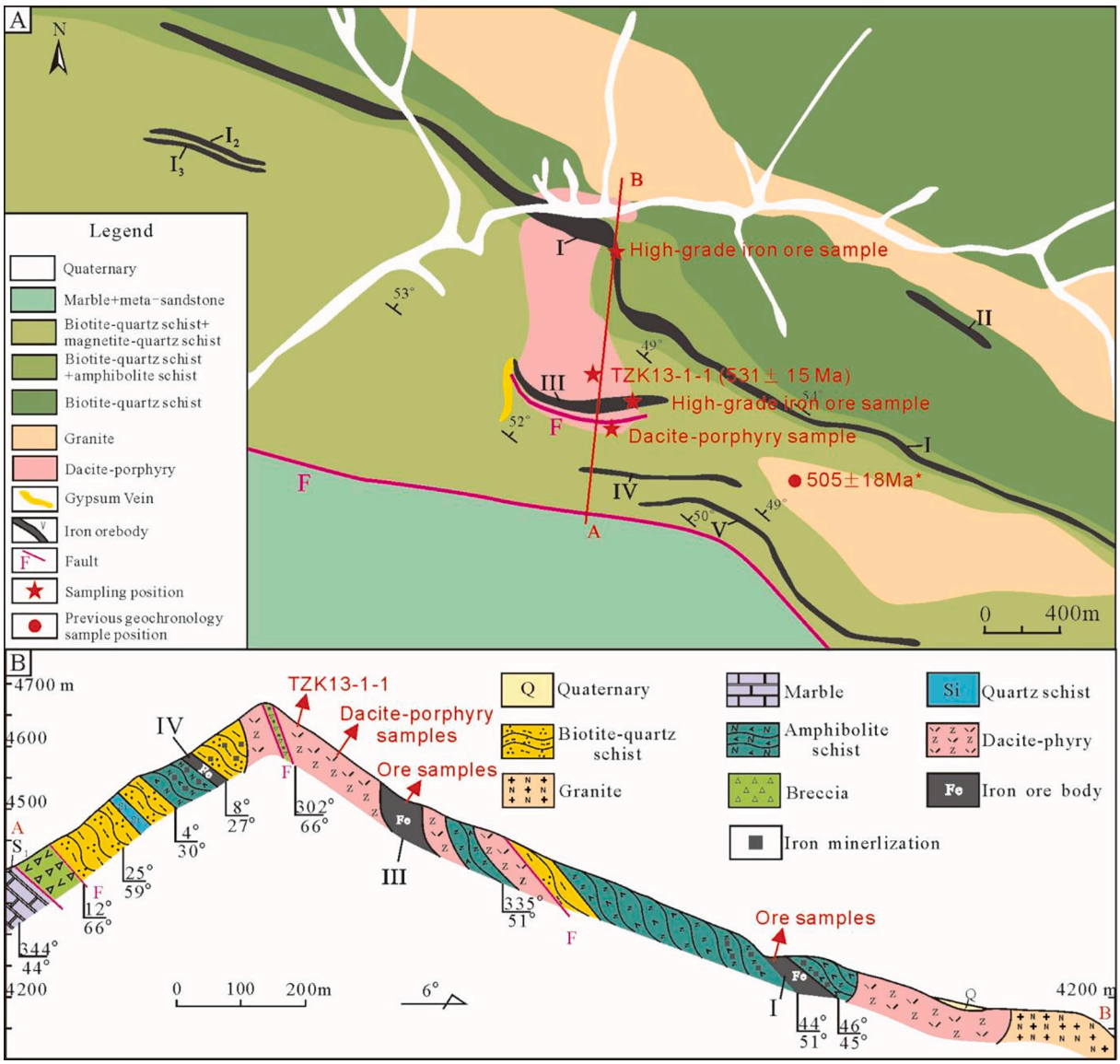

Fig. 2. Geological map and cross section of the prospecting line A-B of the Zankan iron deposit showing the sampling locations in this study, with previous geochronology sample locations from Li (2018) indicated by the red circles in (A).

(Feng et al., 2018).

Previous research has focused on the sedimentary phase of the IFs in the Taxkorgan region, including dating their formation, as well as constraining the source of iron, depositional conditions, and the sedimentary/tectonic settings (Zhou et al., 2017; Zhou et al., 2018; Li et al., 2018a; Li et al., 2019; Hu et al., 2016; Hu et al., 2020, Ding et al., 2021a). For instance, Zhou et al. (2018) determined that the Fe source to the ZID was mainly derived from a mixture of hydrothermal and seawater (hydrogenous) sources. Furthermore, Zhou et al. (2018) considered that the ZID reflects deposition in an early Cambrian seafloor hydrothermal system. Hu et al. (2020) suggested that the ZID is an IF hosted ore deposit, and that variable Eu anomalies in the ores indicate a combination of high- to low-temperature hydrothermal fluids, associated with volcanic events, influenced the entire depositional environment. However, based on earlier geological observations (Li, 2018), such as orebody attitude, wall rock alteration, and contact relations between the orebody and wall rock, it is apparent that the high-grade iron ore in the ZID is a product of the alteration of the primary IF in this region via the circulation of secondary ore forming fluids, and that multiple mineralization stages led to the formation of high-grade ores. Therefore, it is essential to separate the ore forming phases through a combined geological and geochemical study. Here, we provide details of the geologic setting, petrography, and geochemistry of the ZID. Our geological observations are coupled with major and trace element geochemistry of high-grade ore and intrusive dacite-porphyry samples, as well as magnetite oxygen isotopes and pyrite sulfur isotopes. Collectively, our findings allow for a detailed understanding of post-depositional alteration and ore formation in the ZID through the characterization of the ore forming fluid. This, in turn, provides key insights into the processes that resulted in the transformation from the precursor IF to the high-grade ore present in the ZID.

2. Geological background

The WKOB is located towards the southern edge of the Tarim Block, and northern edge of the Karakorum Terrane, at the junction of the Pamir Plateau, Tarim Basin, Central China Orogenic Belt, and Tibetan Plateau. It has previously been demonstrated that the WKOB underwent a protracted period of drift, collision, and subduction of the Proto- and Paleo-Tethys Ocean (Mattern and Schneider, 2000; Xiao et al., 2003, 2005; Jiang et al., 2013; Zhang et al., 2018a). The Oytag-Kegang and Karakorum-Longmucuo-Shuanghu Faults constrain the eastern and

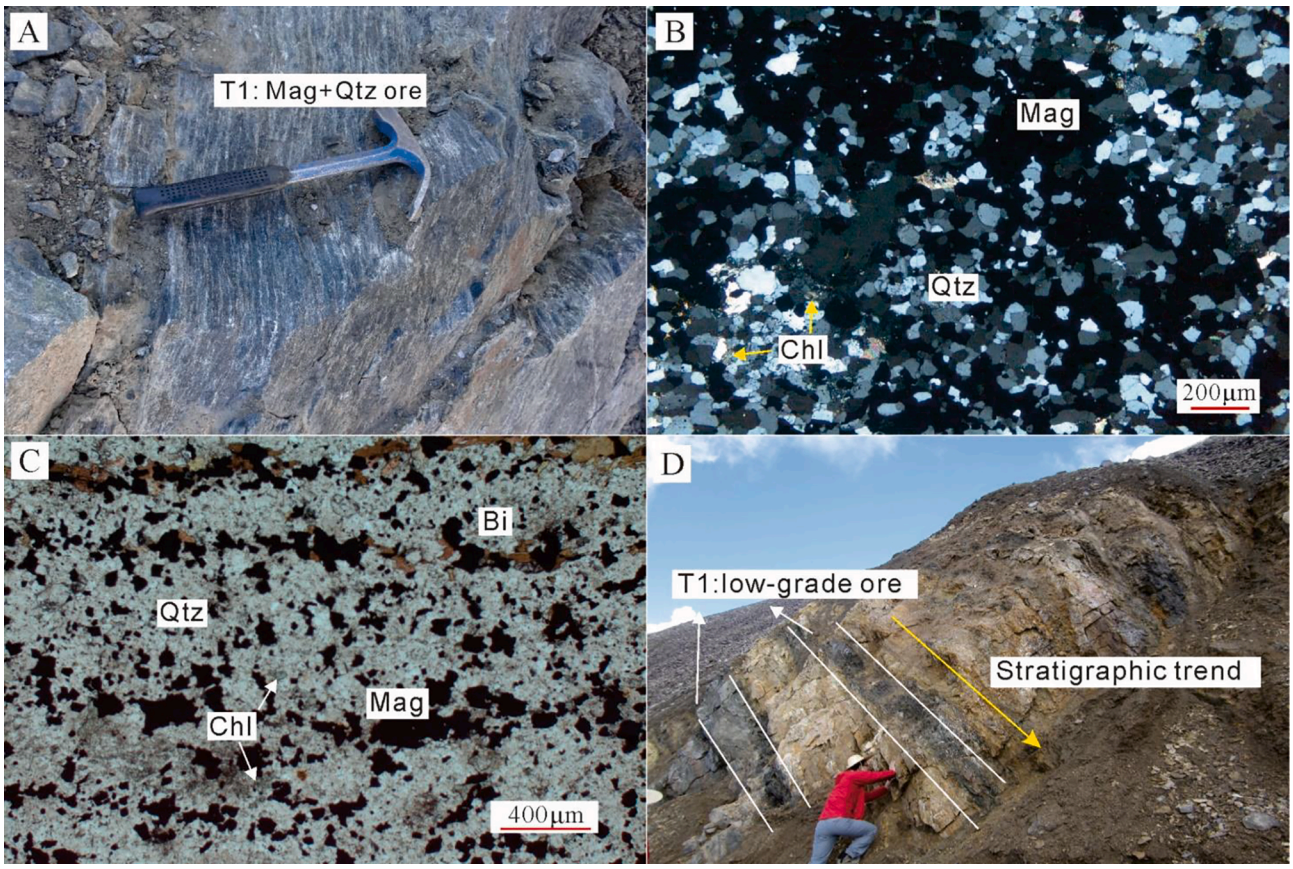

Fig. 3. Field and thin section photographs showing geological characteristics of the T1 ores. (A) Banded structure of T1 ores with magnetite and silica rich bands; (B, C) T1 ores mainly contain magnetite, quartz, biotite, and chlorite; (D) T1 ores have the same trend direction as sedimentary strata; Abbreviations: Bi, biotite; Chl, chlorite; Mag, magnetite; Qtz, quartz.

western boundaries of the WKOB, respectively. Thus, the WKOB can be subdivided into three tectonic units from north to south: the North Kunlun, the South Kunlun, and the Taxkorgan-Tianshuihai Terrane (TTT) (Fig. 1; Pan et al., 1994).

The TTT is bounded by the Kangxiwa Fault to the north and the Taaxi Fault in the south. The faults are oriented NW-SE in the Taxkorgan region, with the field area being dominated by the early Cretaceous Xialafudi Group and the recently defined Cambrian Bulunkuole Group. The Cambrian Bulunkuole Group, deposited between 541.8 and 527 Ma (Li et al., 2019), is the main assemblage in the Taxkorgan terrane that hosts iron and sulfate mineral deposits (Zheng et al., 2018; Peng et al., 2021), while the southern portion of the Bulunkuole Group hosts the largest iron deposit in the region (>160 million metric tons of magnetite ore). Overall, the Bulunkuole Group mainly contains amphibolite schists, biotite-quartz schists, magnetite-quartz schist, sillimanite-garnet schists, marble, and metavolcanics. The corresponding protoliths were most likely graywacke, IFs, bimodal volcanics, carbonates, and sulfates (Zhang et al. 2016; Zheng 2017; Li et al., 2019).

In our study area the Cambrian Bulunkuole Group lacks metavolcanics, and mainly consists of the metasedimentary schists. The IFs in the central mining area of the ZID were intruded by dacite-porphyry, while granite intruded to the southeast and northeast of the ZID (Fig. 2A). A total of five IF-hosted orebodies have been identified in the ZID. Each display both laminated and lenticular structures and they are all interlayered with locally developed metasediments. Orebody I is the largest at nearly 6 km in length and averaging 21.2 m in thickness, while other orebodies are 500 to 1200 m in length and 5 to 20 in thickness. All orebodies have conformable contracts with the aforementioned metasedimentary IFs (Fig. 2B). The strata are monoclinic, trending NW-SE, and dipping to the NE at angles of 25-55°. Low-grade iron ores (TFe < 30%) are mainly hosted in orebodies II, IV and V, while most high-grade ores (TFe > 50 wt%) are developed in the middle parts of the orebodies I and III close to the intrusive rock dacite-porphyry (see section 4.1 for a detailed description of the dacite-porphyry). A Middle Cambrian granite (505 ± 18 Ma; Li, 2018) intrudes the metasediment near orebody IV, but does not have a direct contact with the orebody. The granite near orebody IV contains no magnetite-ferro actinolite veins that are associated with high-grade ores in the ZID, indicating that the high-grade ore forming mechanism occurred prior to the intrusion of the granite.

3. Samples and methods

3.1. Sample descriptions

Seven high-grade iron ore and twelve dacite-porphyry samples were taken from outcrop in the central area of the ZID mining area. Five samples were taken from the No. III orebody and two samples were collected from the No. I orebody. Sampling locations are indicated in Fig. 2. Samples were broken into chips, and any chips with evidence of veins were removed. Selected samples were then ground to a fine powder for major and trace elements analyses. Individual magnetite grains were separated from laminated low-grade magnetite ores and high-grade ores, while disseminated pyrite grains were collected from high-grade magnetite ore samples. Individual mineral grains were further selected under a microscope and prepared for oxygen and sulfur isotope measurements.

Samples earmarked for U-Pb dating were collected from the dacite-porphyry outcrop near the high-grade iron orebodies, with the location noted in Fig. 2. Conventional magnetic and density techniques were used to separate zircons from crushed samples. Zircons were then

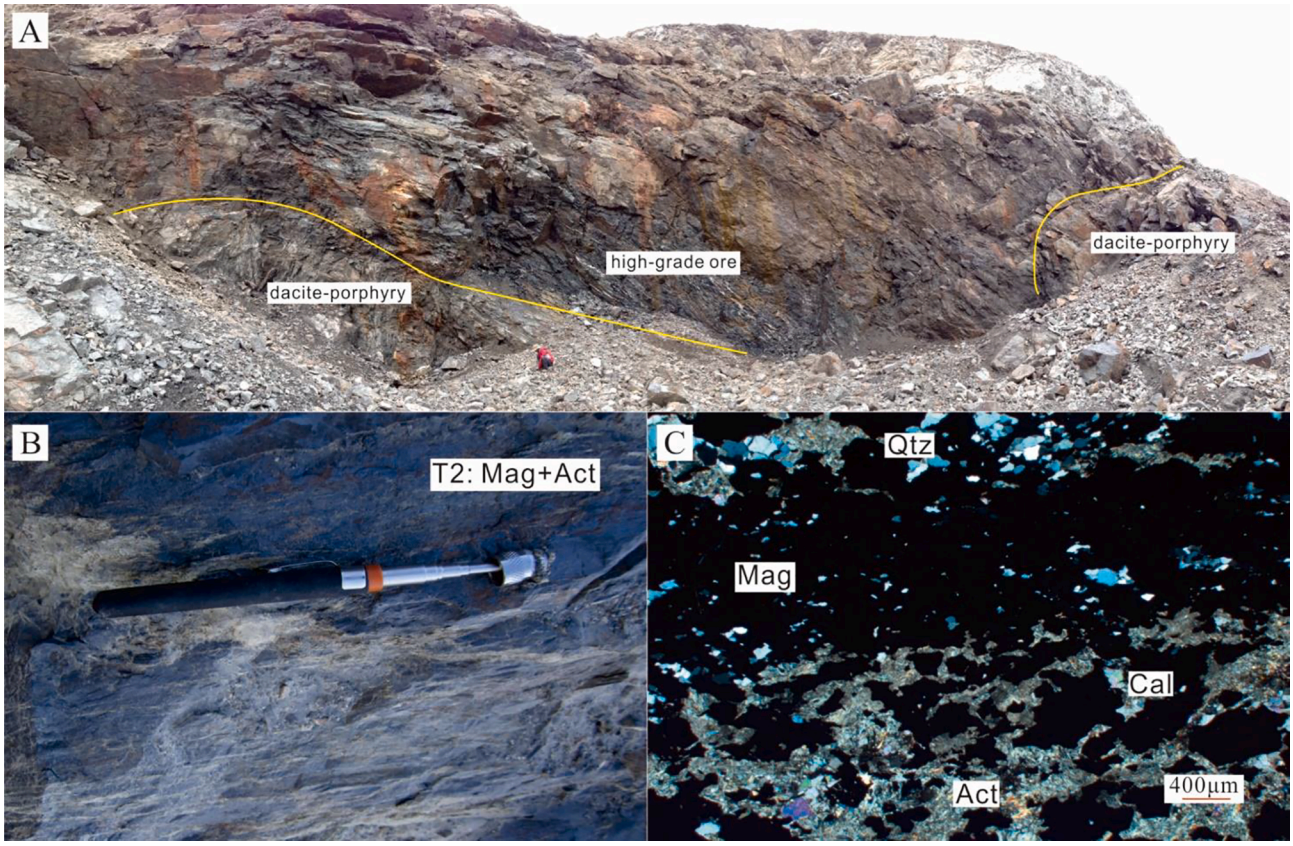

Fig. 4. Field and thin section photographs showing geological characteristics of the T2 ores. (A) The contact between dacite-porphyry and high-grade ore (T2) body, characteristic of an intrusion; (B, C) field and thin section photos showing T2 ores that mainly contain magnetite and ferro actinolite, with minor quartz and calcite. Abbreviations: Act, actinolite; Cal, calcite; Mag, magnetite; Qtz, quartz.

mounted in epoxy resin and polished to section the crystals in half. Transmitted and reflected light micrographs, as well as cathodoluminescence (CL) images, were taken using a CAMECA electron microprobe (EMPA) at the China University of Geosciences (CUGB). The CL images revealed the internal structure and zoning of the zircons. All zircon grains are euhedral to subhedral, 100–150 μm in length, have length to width ratios of 1:2 to 1:3, and show evidence of oscillatory growth (Fig. S1).

3.2. Analytical methods

Major elements for the bulk high-grade iron ore and dacite-porphyry were determined by X-ray fluorescence spectrometry at the Institute of Geology and Geophysics, Chinese Academy of Sciences (IGGCAS). Loss on ignition (LOI) was determined by heating powdered samples at 1000 °C for 2 h and measuring the change in mass. Trace element concentrations were analyzed on an Thermo Scientific Element I inductively coupled plasma-mass spectrometer (ICP-MS) at IGGCAS. Based on the analysis of standards FER-1 and FER-2 external reproducibility is estimated to be 5 to 10%.

Uranium (U) and lead (Pb) isotopes were analyzed on zircon grains via laser ablation ICP-MS (LA-ICP-MS) at the CUGB. Operating conditions included a beam diameter of 32 μm and ablation depth of 20–40 μm. The zircon standard 91,500 was used to assess external reproducibility, and zircon GJ-1 was analyzed as an unknown throughout the entire analytical procedure to monitor external uncertainties. Ratios of $^{207}Pb/^{206}Pb$, $^{207}Pb/^{235}U$, and $^{206}Pb/^{238}U$ were calculated using the program GLITTER. Common Pb corrections were made following Andersen (2002). Calculations of zircon U-Pb isotopic ratios and ages were calculated using the IsoplotR software (Vermeesch, 2018).

The in-situ hafnium (Hf) isotopic composition of dacite-porphyry samples was measured on a Thermo Finnigan Neptune multi-collector ICP-MS (MC-ICP-MS) equipped with a GeoLas-193 laser ablation system at the IGGCAS following the method of Wu et al. (2006). Isobaric interference of ^{176}Lu on ^{176}Hf is negligible due to the extremely low $^{176}Lu/^{177}Hf$ in zircon (normally < 0.002). Measured $^{176}Hf/^{177}Hf$ ratios were normalized to $^{179}Hf/^{177}Hf = 0.7325$. The zircon standard Mud Tank and GJ-1 were analyzed alongside the unknowns. Calculation of εHf(t) values was based on the Hf chondritic value $^{176}Hf/^{177}Hf = 0.282772$ of Blichert-Toft and Albarède (1997). Deviation from a depleted mantle $^{176}Hf/^{177}Hf$ reservoir was calculated assuming a present-day $^{176}Hf/^{177}Hf = 0.28325$, $^{176}Lu/^{177}Hf = 0.0384$ (Griffin et al., 2000), and a decay constant for ^{176}Lu of 1.867×10^{-11} yr^{-1} (Söderlund et al., 2004).

Magnetite grains were separated from the IF and high-grade iron ores using a magnetic separator to a purity >99% at the IGGCAS, then crushed and passed through 200 mesh sieves. Magnetite oxygen isotope analyses were conducted at the Analytical Laboratory of the Beijing Research Institute of Uranium Geology (BRIUG). Oxygen isotope analyses were carried out using the BrF_5 method (Clayton and Mayeda, 1963), where a sample of 12 mg of pure magnetite is reacted with BrF_5 for 15 h to produce oxygen. At 700 °C, the O_2 is then reacted with kryptol and converted to CO_2, collected in a sample tube, and introduced into the inlet of a Finnigan MAT-253 isotope ratio mass spectrometer (IRMS). Oxygen isotope compositions are given in the standard δ-notation and expressed as per mil variations relative to the Vienna standard mean ocean water (VSMOW) standard. Analytical uncertainty is estimated to be 0.2‰.

Individual pyrite samples were separated from ZID high-grade iron ores and then oxidized to SO_2 with CuO. The sulfur isotope composition was measured on a Finnigan MAT-251 IRMS at the BRIUG. Analytical results are expressed relative to the international standard Vienna-

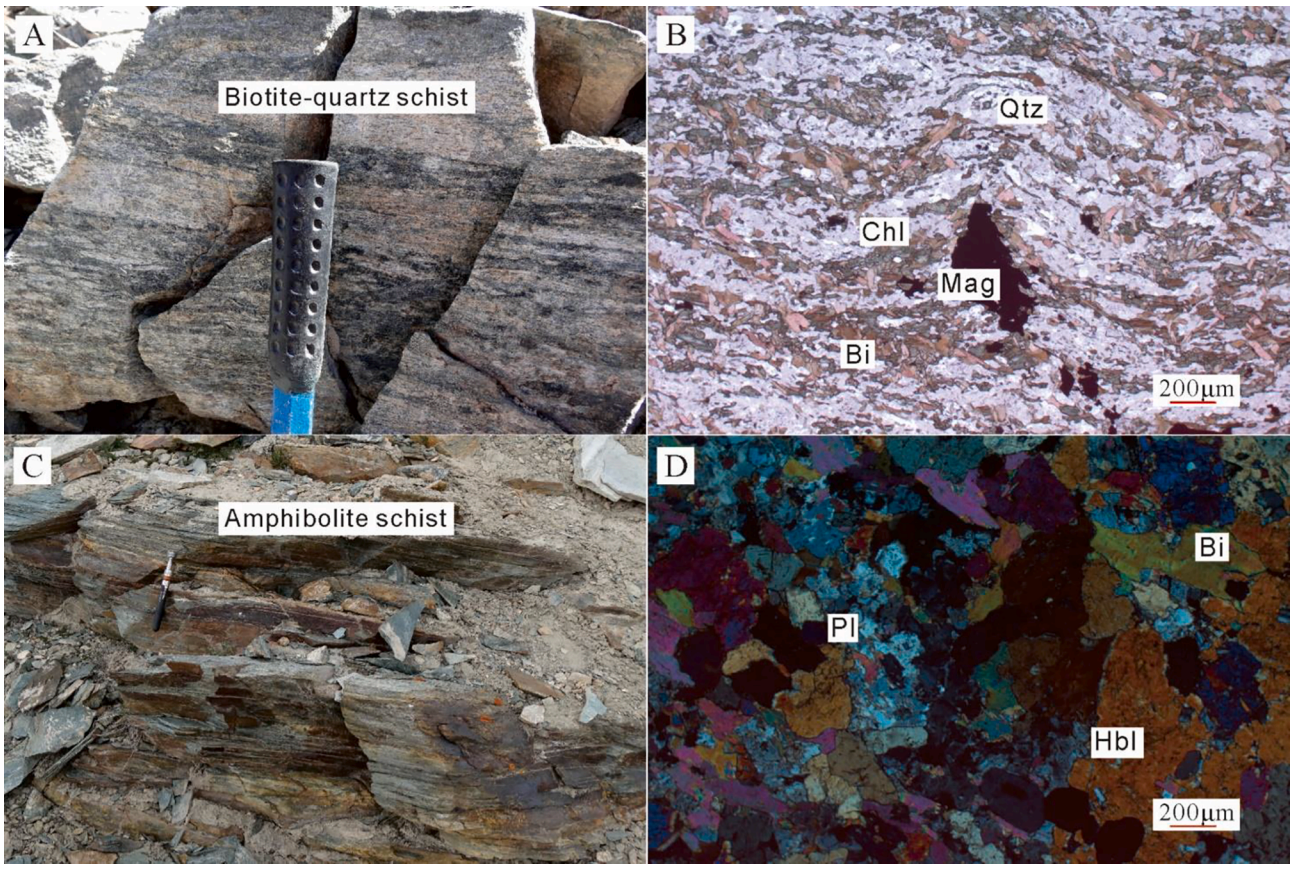

Fig. 5. Field and thin section photographs showing geological characteristics of the main country rocks, (A, B) biotite-quartz schist containing quartz, biotite, chlorite, and minor magnetite grains, and (C, D) amphibolite containing hornblende, plagioclase and biotite. Abbreviations: Bi, biotite; Chl, chlorite; Hbl, hornblende; Mag, magnetite; Pl, plagioclase; Qtz, quartz.

Canyon Diablo Troilite (V-CDT) and precision is estimated to be better than 0.2‰.

4. Results

4.1. Petrography

Based on mineral assemblages, iron ores in the ZID can be classified as two types. Type 1 (T1), a quartz-magnetite ore that is generally low grade (TFe <30 wt%) and hosted in the IF and *meta*-sedimentary rock (biotite-quartz schist and amphibolite schist). It is characterized by banded structures (Fig. 3A) that are parallel to the original sedimentary stratification, and a lack of wall rock alteration. T1 ore is generally composed of 15–40% magnetite, up to 60% quartz, up to 10% biotite and chlorite, and minor calcite (up to 5%) (Fig. 3B, C). This ore type conformably contacts the biotite-quartz schist and amphibolite schist, providing evidence for a sedimentary origin (Fig. 3D). Type 2 (T2) ore is characterized by a higher grade (average TFe = 63 wt%). It is mainly preserved in the central area of the ZID and orebodies I and III, proximal to the dacite-porphyry and associated fracture zones (Fig. 4A). Type 2 ores have massive or banded structures, and contain ferro actinolite (~10%), calcite (~10%), pyrite (~10%), and magnetite (70–90%). Bands in T2 ores are generally magnetite- or ferro actinolite-rich (Fig. 4B, C). A mass of thick quartz veins is developed distally to T2 ore, suggesting that fluid alteration may have leached quartz, leading to the enrichment of magnetite and formation of ferro actinolite during secondary alteration of the host-rocks.

The biotite-quartz schist and amphibolite schist are the main country rocks of the ore bodies in the ZID. The schist is characterized by a fine-grained lepidoblastic texture and is composed of quartz (~40%), biotite (~30%), and chlorite (~20%), along with minor calcite (~5%) and magnetite (~5%) (Fig. 5A, B). The biotite is typically 0.1–1.5 mm in size. Quartz grains display sharp edges indicative of secondary recrystallization by metamorphic fluids during post-depositional alteration. The amphibolite schist is characterized by a lepidoblastic texture and composed of plagioclase and hornblende (~65% and ~ 30%, respectively). Biotite is present as a minor component (~5%) in the amphibolite schist (Fig. 5C, D).

The dacite-porphyry intruded in the central part of the Zankan mining area, and has a porphyritic structure (Fig. 6A). The dacite-porphyry is mainly composed of quartz (40–50%), feldspar (40–60%), and biotite (~10%), with minor hornblende (~3%). The phenocrysts are mainly quartz and feldspar with a size range of 600 to 1000 μm (Fig. 6B, C). The dacite-porphyry contains significant xenocrysts consisting of magnetite, quartz, and biotite, consistent with the original ZID IF mineral assemblage through which it intruded (Fig. 6E, H, I). Furthermore, there are several faults and fracture zones developed in the dacite-porphyry. Most of these structures are filled with magnetite and ferro actinolite, especially near orebodies I and III (Fig. 6D, F, G).

Wall rock alteration is mainly developed near Type II orebodies, as well as the associated structures (e.g., faults). Wall rock alteration shows either actinolitization, carbonatization, pyritization, garnetization, or chloritization (Fig. 7B, C). Actinolitization, developed primarily in the T2 ore, is characterized by the replacement of quartz, biotite, and calcite by ferro actinolite. Some of the T2 ore preserves the original banded structure, however, unlike quartz bands in the T1 ore and IF, ferro actinolite bands are common in the T2 ore. Carbonatization is present within the T2 ore and is associated with magnetite, quartz, and ferro actinolite near the fracture zones. Some calcite displays vein structures that crosscut the original magnetite bands. Pyritization developed in the

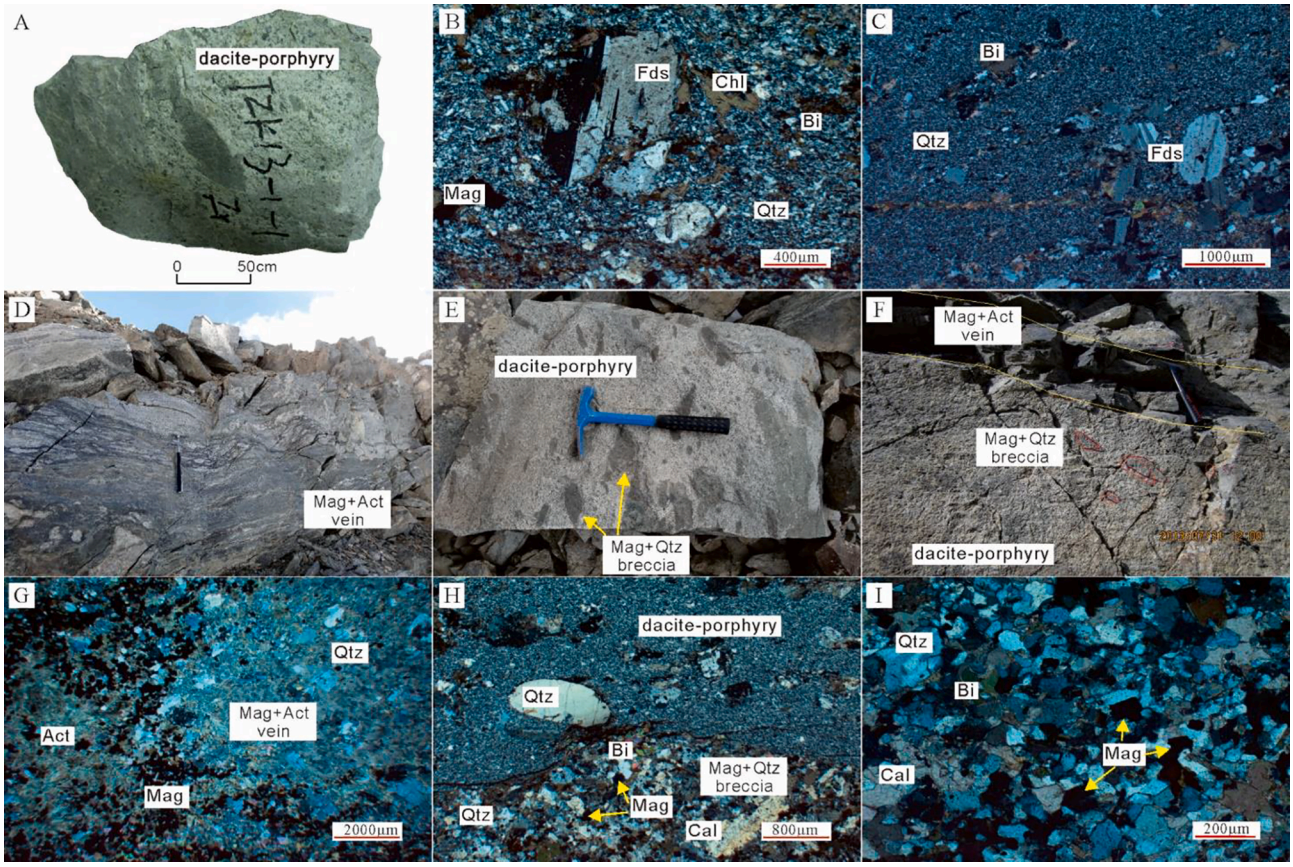

Fig. 6. Field and thin section photographs of the dacite-porphyry in the ZID. (A) Hand sample of the dacite porphyry; (B, C) phenocrysts in the dacite are mainly feldspar and quartz; (D) fracture zone within dacite porphyry filled with magnetite-ferro actinolite; (E) dacite porphyry containing primary IF xenocrysts; (F) magnetite-quartz xenocrysts and magnetite-ferro actinolite veins within the dacite-porphyry indicating a two stage mineralization; (G) magnetite-ferro actinolite veins containing residual quartz; (H) boundary between the magnetite-quartz xenocrysts, showing a similar mineral assemblage as T1 ores and primary IF, and the dacite porphyry. Abbreviations: Act, ferro actinolite; Bi, biotite; Cal, calcite; Chl, chlorite; Fds, Feldspar; Mag, magnetite; Qtz, quartz.

T2 ore displays disseminated or veined structures. Pyrite grains are generally present as subhedral to anhedral crystals and are dispersed between magnetite grains (Fig. 7D). Alternatively, pyrite grains are present filling in the fracture zone or as minor pyrite veins. Collectively, these textural features indicate pyrite formed through post-depositional alteration. Garnetization and chloritization and are highly associated with the dacite porphyry, and are mainly developed in the most altered zones such as those proximal to faults in the dacite porphyry.

4.2. Major and trace element abundances

4.2.1. High-grade ores

Major and trace element compositions of the T2 ore are listed in Table 1, and for comparison, provide T1 ore values for the ZID (Li et al., 2018b). The T2 ore is characterized by high TFe (52.7–72.3 wt%, average 63.4 wt%) and SiO_2 (3.49–17.06 wt%, average 8.75). Other major elements are present at relatively low concentrations: 0.48–8.69 wt% (CaO), 0.56–3.45 wt% (MgO), and 0.23–2.55 wt% (P_2O_5). Further, Al_2O_3, TiO_2, MnO, Na_2O, K_2O are general very low in the T2 ore. REE concentrations, have high total REE + Y concentrations (ΣREE + Y; average 556.03 ppm), while the T1 ores have average 157.93 ppm of ΣREE + Y. Europium (Eu) concentration in the T2 ore averages 1.76 ppm (0.28–4.17 ppm), similar to the T1 ores (average 1.96 ppm). All T2 ore samples display a negative Eu anomaly (0.36–0.57) in chondrite normalized plots (Fig. 8A); however, T1 ore samples display flat REE + Y patterns.

4.2.2. Dacite-porphyry

The dacite-porphyry in the study areas displays a relatively consistent chemical compositions (Table 2), with high SiO_2 (68.85–73.47 wt %) and $TiO_2 + Al_2O_3$ (13.47–14.03 wt%) contents, along with a moderate alkali component $Na_2O + K_2O$ (7.25–7.89 wt%) and CaO (1.17–2.97 wt%). MgO, P_2O_5, and MnO are generally present at abundances of < 1 wt%. Whole rock geochemistry indicates the dacite-porphyry falls in the subalkaline fields of both SiO_2-Zr/TiO_2 and SiO_2-Nb/Y diagrams (Fig. 9A, B; Winchester and Floyd, 1977), and the calc-alkaline volcanic rock field on a Zr-Y diagram (Fig. 9C; Ross and Bédard, 2009). When viewed on a chondrite normalized plot (Fig. 8C), the dacite-porphyry is depleted in heavy rare earth elements (HREEs). Further, the dacite-porphyry is characterized by La/Yb_N ratios between 3.83 and 8.65, consistent with light rare earth element (LREE) enrichment, and prominent negative Eu anomalies (0.44–0.73). Similarly, the dacite-porphyry is enriched in large-ion lithophile element (LILEs) and depleted in high field strength elements (HFSEs) (e.g., Nb, Ta, and Ti) (Fig. 8D).

4.3. Geochronological and Hf isotope results

The zonation observed, along with Th/U ratios of 0.43–0.77, indicates a magmatic origin (Corfu et al., 2003; Pupin, 1980). Among fifteen zircons collected from the geochronology sample, fourteen yield an apparent $^{206}Pb/^{238}U$ age of 475 to 580 Ma. One zircon measured at both its core and rim yielded ages of 942 Ma and 574 Ma, respectively, suggesting an older zircon was captured during the younger magmatic events (Table. 3). Concordia diagrams indicate that there are two

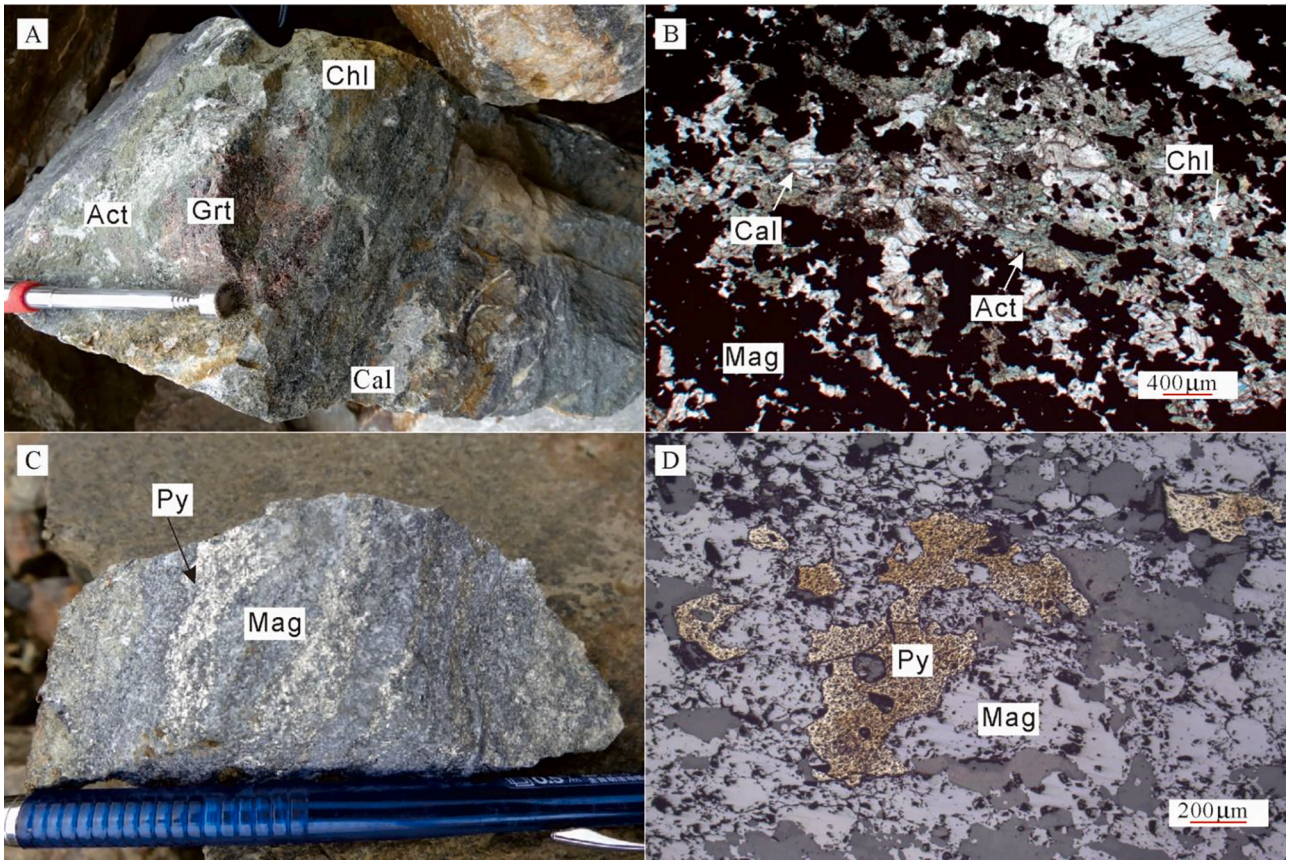

Fig. 7. Hand sample and thin section photographs of wall rock alteration near the high-grade ore. (A, B) Wall rock alterations such as actinolization, garnetization, carbonatization, and chloritization. (C, D) Pyritization in the T2 ores. Abbreviations as in Fig. 3. Abbreviations: Act, ferro actinolite; Cal, calcite; Chl, chlorite; Grt, garnet; Mag, magnetite; Py, pyrite.

separate groups of zircons based on age (Fig. 10A). One group yields an age of 497.82 ± 3.81 Ma (MSWD = 0.63, n = 6) while the other group yields an age of 551.25 ± 3.32 Ma (MSWD = 5.5, n = 8). (Fig. 10B, C). Furthermore, twelve $^{176}Hf/^{177}Hf$ ratios ranging from 0.282280 to 0.282540 were obtained from dacite-porphyry zircons (Table. 4), in good accordance with the recommended values for MC-ICP-MS analysis (Woodhead and Hergt, 2005).

4.4. Sulfur and oxygen isotope results

The oxygen isotope composition ($\delta^{18}O_{VSMOW}$) of the magnetite from T1 and T2 ores range from 1.8 to 3.2‰, and 4.4 to 5.5‰, respectively (Tables 5). It should be noted that there are two group of samples, from localities only two meters apart (e.g. ZK12-346/ ZK12-348, and ZK42402-86/ZK42402-88), however, the oxygen isotope fraction of the magnetite between T1 and T2 ores is 1.2‰ and 1.7‰, providing strong evidence that the magnetite from both types of ores may be discriminated.

The $\delta^{34}S_{V\text{-}CDT}$ values of pyrite grains from the T2 ore range from 19.1 to 27.3‰ (Tables 6), consistent with a recent study on the ZID (17.2 to 29.89‰, Ding et al., 2021b). The highest pyrite $\delta^{34}S_{V\text{-}CDT}$ value is close to that of Cambrian seawater sulfate ($\delta^{34}S_{V\text{-}CDT}$ = 30 ± 3‰, Kampschulte and Strauss, 2004), and all samples have $\delta^{34}S_{V\text{-}CDT}$ values higher than mantle, suggesting a non-magmatic origin such as meteoric waters.

5. Discussion

5.1. Iron mineralization and the dacite-porphyry intrusion

Previous studies have demonstrated that the ZID host is mainly a *meta*-sedimentary sequence, whose maximum depositional age is constrained to 540 Ma based on the age distribution for a population of detrital zircons (Li et al., 2019). However, the minimum age of the ZID remains debated, with estimates ranging from 541.8 to 505 Ma (Li, 2018; Ding et al., 2021a). Here, the older age group of zircons from the dacite porphyry (551.25 ± 3.32 Ma) indicates that the magma captured recycled zircons from the original sedimentary strata, consistent with the age provided by the previous youngest detrital zircon group in the Zankan area (Li, 2018). The older zircons share a similar morphology with the magmatic zircons, indicating that they are most likely sourced from igneous rocks undergoing weathering, similar to the surrounding area, Jiertieke (Li et al., 2018a,b).

The granite southeast of the ZID, which intrudes the ore-hosting strata near orebody IV, has been previously dated to 505 Ma ± 18 Ma (Li, 2018). Given the absence of magnetite-ferro actinolite veins in the granite and the older age, the younger zircon group age (497.82 ± 3.81 Ma) is interpreted here to reflect the formation age of the T2 ores in the ZID. This is supported by the fracture zone in the dacite-porphyry being filled with magnetite-ferro actinolite, which corresponds to the second stage of ore formation (Fig. 6D, F). Collectively, these results point to the formation of T2 ore within the ZID occurring after 497.82 Ma.

5.2. Tectonic considerations

5.2.1. Element mobility

Dacite-porphyry from the ZID exhibit LOI values of 0.06–0.19 wt% and are characterized by a very low-degree of alteration. Therefore, trace elements, such as REE and HFSEs (e.g., Nb, Ta, Zr, Hf, Ti, Th) in the dacite-porphyry, can be considered immobile during this alteration (Barnes et al., 1985; Winchester and Floyd, 1977). Additionally, all

Table 1
Major and trace elements in T1 and T2 iron ore samples from the Zankan iron deposit.

	TZK13-3–1	TZK13-3–3	TZK11-2	TZK11-3	TZK11-4	ZK504-14	ZK12-382	TZK5-1	TZK5-4	TZK5-5
Ore type	T2 ores							T1 ores		
location	No. III orebody					No. I orebody		No. V orebody		
SiO_2	16.20	3.49	4.30	9.60	4.97	17.06	5.66	40.43	42.77	44.3
TiO_2	0.09	0.22	0.62	0.63	0.87	0.36	0.03	1.59	0.83	0.97
Al_2O_3	0.93	1.03	1.37	0.69	0.46	1.50	0.37	11.21	8.95	9.42
ΣFeO	72.80	93.50	91.17	72.71	84.99	67.73	87.82	20.47	21.35	19.42
MnO	0.21	0.07	0.09	0.31	0.30	0.58	0.16	0.28	0.3	0.3
MgO	2.66	0.56	0.81	2.70	0.74	3.45	0.61	4.52	5.95	5.85
CaO	4.56	0.48	0.85	8.69	4.42	7.61	1.50	9.1	9.65	9.91
Na_2O	0.28	0.24	0.33	0.09	0.12	0.44	0.02	2.14	2.42	1.95
K_2O	0.04	0.09	0.07	0.02	0.08	0.07	0.01	2.12	0.49	1.64
P_2O_5	1.55	0.23	0.28	2.34	2.55	0.71	0.62	0.29	0.16	0.24
LOI	0.32	<0.10	<0.10	2.12	0.10	0.10	2.63	7.75	7.04	5.88
TOTAL	99.64	99.91	99.91	99.89	99.61	99.51	99.43	99.9	99.91	99.88
FeO	16.28	17.08	18.27	18.18	–	–	–	6.13	5.94	5.84
Rb	3.35	0.63	2.43	0.30	2.65	1.33	0.37	104.2	19.9	112.3
Ba	14.60	7.21	12.65	7.96	19.10	52.29	30.99	1000	105	3119.7
Th	2.58	7.91	2.77	9.37	5.55	16.23	2.58	2.01	0.55	4.65
U	1.13	1.44	2.18	4.86	1.50	1.24	1.52	2.08	1.04	7.96
Ta	0.04	0.10	0.09	0.18	0.02	0.05	0.14	0.41	0.26	0.48
Pb	1.11	1.60	1.28	1.94	0.96	13.47	1.31	10.7	15.2	10.7
Sr	2.88	17.94	7.62	35.62	18.51	30.79	12.94	131.1	135.3	134
Nb	1.58	1.35	2.90	2.61	0.02	1.11	3.21	6.02	3.83	6.43
Zr	5.11	5.20	5.23	3.59	0.49	3.06	0.17	4.25	8.42	4.64
Hf	0.16	0.10	0.15	0.07	0.11	0.16	0.03	0.21	0.37	0.11
La	16.56	89.17	24.92	180.74	163.49	83.72	62.08	22.1	12.9	30.1
Ce	32.77	212.70	51.25	374.62	366.39	184.61	126.65	50.1	21.6	44.9
Pr	3.95	26.14	6.20	44.19	42.47	21.31	14.70	7.64	2.86	5.28
Nd	15.02	102.93	24.59	176.02	182.77	79.32	58.43	35.4	14	22.4
Sm	2.73	18.55	4.59	33.76	42.13	13.50	11.06	8.02	4.39	5.14
Eu	0.28	1.94	0.52	4.17	3.36	1.29	0.77	2.86	1.36	1.65
Gd	2.63	17.64	4.25	37.24	40.58	12.72	10.14	8.42	5.42	5.72
Tb	0.38	2.51	0.63	6.33	6.24	2.03	1.54	1.41	1.05	0.97
Dy	1.91	13.35	3.55	40.14	32.17	11.58	8.27	8.62	6.65	5.77
Y	10.41	61.76	17.81	236.19	136.84	66.96	41.97	42.3	35.8	30.6
Ho	0.40	2.69	0.75	9.05	6.34	2.83	1.75	1.79	1.4	1.19
Er	1.06	6.70	1.99	24.43	15.62	8.37	4.99	4.62	3.56	3.07
Tm	0.17	0.86	0.28	3.37	1.97	1.22	0.68	0.64	0.5	0.44
Yb	0.98	5.07	1.79	20.09	12.67	8.93	4.76	3.81	3.08	2.78
Lu	0.15	0.72	0.28	2.94	1.98	1.48	0.78	0.52	0.47	0.41
∑REE + Y	89.40	562.74	143.39	1193.25	1055.00	499.86	348.56	198.3	115	160.5

* Li et al. (2018b).

samples display consistent immobile and mobile element patterns (Fig. 8). Accordingly, REEs and HFSEs are discussed below to characterize the dacite-porphyry with respect to their original chemical composition and the possible tectonic environment during formation.

5.2.2. Genetic type of dacite-porphyry

Generally, granites and dacites may be divided into three genetic types: I-, S- and A-types. This classification is based on a combination of source characteristics and tectonic affinities, with I-type representing subduction, S-type being continental collision and A-type being oceanic spreading or rifting (Chappell and White, 1992; Whalen et al., 1987). The dacite-porphyry in the study area is alkaline, lacking primary peraluminous minerals such as muscovite, garnet, or cordierite. This composition would be inconsistent with a strongly felsic and peraluminous S-type granite (Chappell and White, 1992). Classification as an A-type granite is also unsuitable because the studied dacite-porphyry has low ΣFeO/MgO (2.25–4.57) ratios and lacks any of the characteristic minerals for A-type volcanic rocks. All samples have 10,000*Ga/Al ratios that fall between 2.07 and 2.83, with an average of 2.38. This is below the minimum value of 2.6 that characterizes A-type granites but is consistent with expected values for I-type granites (Fig. 9; Whalen et al., 1987). Given the relatively low Zr, Nb, Ce, and Y concentrations, most samples fall into the fields that represent fractionated and unfractionated granites, highlighting their transitional character. Given these observations, the Cambrian dacite-porphyry can be classified as an I-type igneous rock, although, a small component of these rocks may also represent contributions from fractionated melts derived from an initial calc-alkaline magma (Fig. 9C).

5.2.3. Source characteristics of igneous rock

Zircon Hf isotopes are an excellent geochemical tracer for magma sources and petrogenetic process, and offer insights into the nature of crustal evolution (Kinny and Maas, 2003). Dacite-porphyry zircons have $\varepsilon_{Hf}(t)$ values from −6.1 to 4.6, which plot below the depleted mantle (DM) lines and towards the crustal evolution lines (Fig. 11). Two-stage Hf model ages (T_{DM2}) vary from 1866 to 1239 Ma, amongst which the negative $\varepsilon_{Hf}(t)$ values generally correspond to younger T_{DM2} ages. Zircons with U-Pb ages of 580 to 494 Ma in the dacite-porphyry correspond with variable T_{DM2} ages between 1239 and 1866 Ma, much older than their crystallization ages. This suggests that the zircons were derived by melting ancient crustal materials that were extracted from the mantle ca. 1.8–1.2 Ga. Consequently, it can be inferred that the primary magmas that formed the Cambrian volcanic rocks in the study area were generated through the partial melting of Paleoproterozoic to Mesoproterozoic crustal material.

5.2.4. Tectonic setting

Bimodal volcanics in the Cambrian Bulunkuole Group indicate an extensional event in the Taxkorgan region about 521 Ma (Zheng et al., 2018). However, others have argued that the regional volcanic-sedimentary sequence represents an early Paleozoic accretionary wedge formed by the subduction of the Proto-Tethys Ocean under the

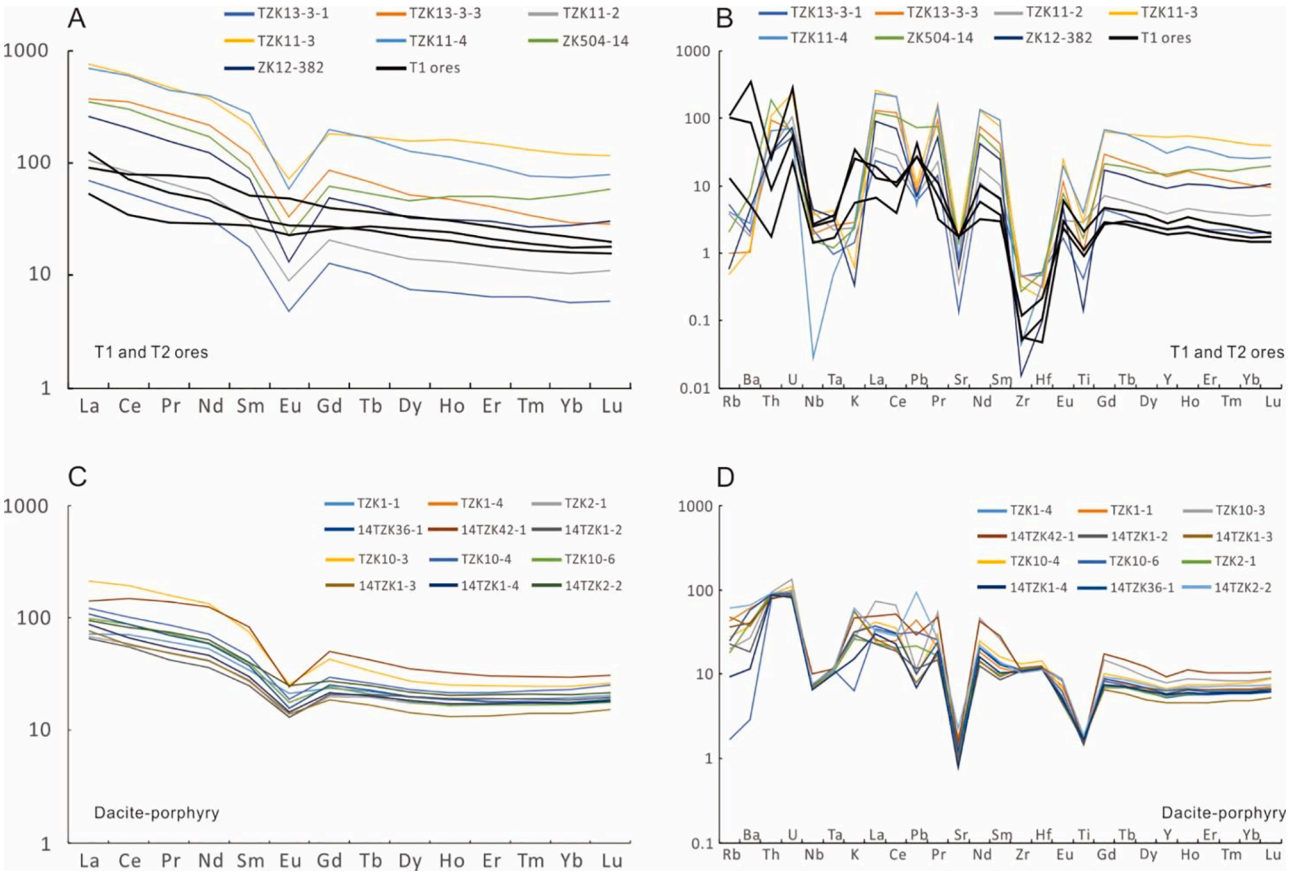

Fig. 8. Chondrite-normalized REE patterns (A, C) and primitive-mantle-normalized spider diagrams (B, D) for the Zankan T1, T2 ores and dacite-porphyry. Chondrite and primitive mantle normalizing values are from Sun and McDonough (1989).

TTT (Zhou et al., 2017; Zhang et al., 2018a, 2018b, 2019). Here, we consider that the presence of the 497.82 Ma dacite-porphyry in the ZID, an I-type volcanic unit, was mainly developed in a continental arc volcanic setting where the Proto-Tethys ocean plate was subducted under the TTT. Therefore, the Taxkorgan region was dominated by an active continental margin in the middle Cambrian (e.g., Li et al., 2019; Zhang et al., 2018a, 2018b, 2019). As such, the extensional rift should be before a subduction-related arc system along the continental margin, and the ZID would have been influenced by the continental arc volcanism (Fig. 12). Persistent volcanic and magmatic actives in the region would have resulted in significant hydrothermal input to the basin, which would have generated the conditions necessary for the alteration of the IF and development of the T2 ore.

5.3. Genesis of high-grade iron ores in the ZID

The magnetite-quartz xenocrysts and high-grade iron veins in the 497.82 Ma dacite-porphyry indicate that the ZID may have experienced two stages of metallogenesis. The first stage involved deposition of the original IF with typical sedimentary features such that all orebodies are controlled by the sedimentary strata. The protolith of the country rock (biotite-quartz schist) is sedimentary in origin (Li et al., 2019), and T1 ore display banded structures that parallel the sedimentary strata. However, the T2 ore lack sedimentary features, and is associated with the fracture zones near the dacite-porphyry. The T1 ore within the ZID display flat chondrite normalized REE patterns with no discernable anomalies (Fig. 8), as well as relatively heavy oxygen isotope values ($\delta^{18}O$ = 4.4 to 5.5‰). T2 ore, on the other hand, displays negative Eu anomalies and lighter oxygen isotope values ($\delta^{18}O$ = 1.9 to 3.2‰), suggesting that significantly different geochemical processes led to the mineralization of T1 and T2 ores. This further supports the interpretation that the T2 ore formed as the result of post-depositional alteration and not associated with the sedimentary stage. This finding is consistent with Thorne et al. (2009) who demonstrated that iron oxides from altered IF and high-grade iron ores in the Hamersley Province, Western Australia, are characterized by much lighter $\delta^{18}O$ values than unaltered IF. Additionally, Li et al. (2015) demonstrated that IF-hosted high-grade iron ore in the Anshan area (China) similarly display lighter $\delta^{18}O$ values when compared to low-grade ore bodies, indicating alteration by a $\delta^{18}O$ depleted water possibly derived from meteoric water. Therefore, the T2 ore in the ZID likely reflect post-depositional fluid alteration of the T1 ore and initial IF.

To further understand the mechanism(s) that generated the high-grade iron ores, it is essential to investigate the characteristics of the ore forming fluids. Rare earth elements and isotopic signals can provide unique insights into potential hydrothermal activities that may have altered the T1 ore and IF within the ZID. T2 ore and dacite-porphyry samples share similar chondrite-normalized REE patterns that are characterized by LREE enrichment and negative Eu anomalies. Similar trace element compositions and REE patterns in the T2 ore and dacite-porphyry suggest that the mineralizing fluid may be associated with; (a) the dacite-porphyry magma, or (b) a non-magmatic fluid that leached trace elements from the dacite-porphyry and deposited metals in the T2 ore (Zhou et al., 1994).

Previous work has considered that sulfur in the Zankan pyrites was sourced from a mixture of hydrothermal fluids and ambient seawater (Zhou et al., 2018). To further distinguish the source of the high-grade iron ore mineralization fluid, we analyzed sulfur isotopes in pyrite from T2 ore. The sulfur isotopes are characterized by heavier $\delta^{34}S_{V\text{-}CDT}$ values that range from 19.1‰ to 28.2‰, with an average of 23.4‰. This is significantly heavier than the primitive mantle (0 ~ 3‰; Kusakabe et al., 1990) but close to estimates for contemporaneous seawater of

Table 2
Major and trace elements in dacite-porphyry samples from the Zankan iron deposit.

	TZK1-1	TZK1-4	TZK2-1	TZK10-3	TZK10-4	TZK10-6	14TZK36-1	14TZK42-1	14TZK1-2	14TZK1-3	14TZK1-4	14TZK2-2
SiO_2	68.85	70.91	71.24	73.37	73.47	70.89	72.10	68.76	68.78	71.20	70.91	66.20
TiO_2	0.38	0.36	0.34	0.33	0.31	0.34	0.32	0.34	0.39	0.36	0.36	0.40
Al_2O_3	13.65	13.60	13.47	13.14	13.38	13.24	13.22	13.07	14.01	13.90	13.60	13.59
ΣFeO	4.58	3.79	3.08	3.05	2.87	2.91	2.51	4.88	4.12	3.91	3.79	5.80
MnO	0.11	0.06	0.08	0.06	0.05	0.07	0.06	0.11	0.05	0.04	0.06	0.15
MgO	1.13	1.00	1.14	0.91	0.83	1.05	0.92	1.95	0.85	0.77	1.00	1.40
CaO	2.97	1.72	2.01	1.33	1.17	2.52	1.48	2.68	1.87	1.08	1.72	3.62
Na_2O	5.56	7.43	6.73	6.58	6.61	7.58	6.29	5.41	7.14	5.72	7.43	5.30
K_2O	1.69	0.46	0.78	0.78	0.93	0.19	0.95	1.38	0.87	1.67	0.46	1.83
P_2O_5	0.08	0.12	0.04	0.13	0.06	0.08	0.09	0.07	0.10	0.09	0.12	0.11
LOI	0.09	0.06	0.11	0.12	0.10	0.13	0.19	0.12	0.15	0.13	0.06	0.10
TOTAL	99.09	99.51	99.02	99.80	99.78	99.00	98.13	98.77	98.33	98.87	99.51	98.50
Sc	8.84	6.23	10.93	10.06	5.24	5.04	10.33	12.16	9.01	9.52	8.84	16.88
V	135.10	112.02	106.09	82.29	74.45	68.14	60.69	116.15	147.12	123.85	135.10	132.89
Cr	5.64	6.81	166.54	136.24	135.22	131.18	140.42	132.95	8.64	11.76	5.64	16.77
Co	3.59	1.23	3.87	2.83	1.97	3.28	2.47	5.12	7.96	5.68	3.59	2.19
Ni	1.28	3.55	9.03	14.18	42.23	49.71	12.88	21.37	20.21	10.93	−1.28	14.40
Cu	0.81	0.06	6.72	6.57	16.88	20.00	4.68	6.05	10.81	5.78	0.81	5.31
Zn	5.21	9.20	6.80	7.05	7.66	6.66	6.59	7.98	6.25	6.93	5.21	13.51
Ga	15.48	16.36	18.31	19.68	14.64	17.14	16.74	17.65	17.75	17.21	15.48	17.57
Rb	5.87	27.05	12.72	17.31	1.05	11.46	15.77	23.11	14.34	30.37	5.87	38.71
Sr	16.67	37.37	23.76	28.21	19.83	31.58	25.20	31.42	20.33	18.44	16.67	47.18
Y	25.82	26.24	36.24	30.38	23.83	24.44	26.88	42.00	28.86	20.67	25.82	29.37
Zr	120.49	117.02	125.57	149.42	125.58	130.01	121.92	121.59	123.57	132.98	120.49	116.78
Nb	4.63	5.07	5.10	5.35	5.20	4.84	5.30	7.14	5.06	5.13	4.63	5.47
Ba	79.95	421.58	188.59	260.97	19.94	283.37	399.12	280.91	127.21	259.63	79.95	461.65
La	20.85	17.04	50.19	28.88	23.43	16.15	25.82	33.63	15.49	18.18	20.85	22.39
Ce	40.72	43.47	117.74	62.13	53.46	36.26	53.92	90.77	33.69	35.37	40.72	50.44
Pr	5.18	5.83	15.18	8.24	6.94	4.57	6.67	13.29	4.04	4.63	5.18	7.13
Nd	21.58	24.64	62.33	33.76	27.89	19.18	27.51	58.51	16.89	19.41	21.58	29.79
Sm	4.59	5.24	11.46	7.02	6.04	4.31	5.77	12.73	3.81	4.18	4.59	6.18
Eu	0.84	1.23	1.49	1.09	1.03	0.75	0.91	1.41	0.76	0.81	0.84	1.44
Gd	4.47	4.87	8.83	6.09	5.02	4.13	5.21	10.34	4.29	3.85	4.47	5.60
Tb	0.76	0.82	1.27	0.99	0.78	0.73	0.85	1.59	0.77	0.63	0.76	0.93
Dy	4.69	5.00	6.92	5.86	4.57	4.45	5.07	8.92	5.09	3.64	4.69	5.57
Ho	0.98	1.06	1.44	1.23	0.94	0.95	1.07	1.84	1.09	0.75	0.98	1.17
Er	2.84	3.14	4.14	3.58	2.76	2.82	2.98	5.02	3.17	2.22	2.84	3.44
Tm	0.45	0.49	0.63	0.57	0.43	0.45	0.46	0.76	0.49	0.36	0.45	0.53
Yb	2.99	3.31	4.16	3.91	2.90	3.03	3.03	5.04	3.17	2.41	2.99	3.54
Lu	0.46	0.52	0.67	0.65	0.45	0.49	0.48	0.78	0.50	0.39	0.46	0.55
Hf	3.55	3.49	3.81	4.50	3.69	3.86	3.69	3.64	3.75	3.92	3.55	3.51
Ta	0.41	0.44	0.49	0.47	0.46	0.43	0.49	0.48	0.49	0.48	0.41	0.46
Tl	0.10	0.39	0.19	0.23	0.08	0.17	0.14	0.31	0.18	0.18	0.10	0.45
Pb	1.27	8.05	2.10	1.82	5.78	4.02	1.87	5.42	2.15	1.48	1.27	17.57
Bi	0.03	0.07	0.01	0.00	0.07	0.02	0.01	0.01	0.08	0.04	0.03	0.09
Th	7.37	7.09	8.05	7.57	6.67	7.83	7.62	6.87	7.45	7.27	7.37	7.86
U	1.72	2.11	2.82	2.32	1.91	1.66	2.03	1.84	1.93	1.71	1.72	2.05

$\delta^{34}S_{V\text{-}CDT} = 30 \pm 3‰$ (Kampschulte and Strauss, 2004). Therefore, it is unlikely that the high-grade iron ore forming fluid was directly derived from the magma.

Oxygen isotope analyses further indicate that the high-grade ore mineralization fluid was not magmatically sourced but instead derived from ^{18}O-poor meteoric water (Li et al., 2015). Even though the evidence of sedimentary sulfate formation in the ZID remains enigmatic, in areas proximal to the ZID (i.e., those from the same basin) there are several Cambrian formations that are sulfate-rich, such as the Kalaizi barite formation and the Laobing anhydrite formation (Fig. 1C; Zheng et al., 2018). The presence of these formations would imply that the basin was enriched in sulfate. In the ZID, some of the fracture zones are filled with gypsum (Fig. S2), indicating that the fluid carried dissolved marine sulfate and transported this sulfate into the fracture zone. During the transportation, either microbial sulfate reduction and thermochemical sulfate reduction would have generated an isotopically heavy reservoir of residual dissolved SO_4^{2-} (Yan et al., 2020), and an isotopically light flux of S^{2-}, leading to the $\delta^{34}S_{pyrite}$ that are lower than coeval seawater but higher than $\delta^{34}S_{gypsum}$ values. This is consistent with a previous study on gypsum in the ZID ($\delta^{34}S_{gypsum} = 35.8 \sim 37.1‰$, Chen, 2012) and findings on $\delta^{34}S_{pyrite}$ presented here. Alternatively, if infiltrating meteoric water came into contact with the dacite-porphyry magma chamber, additional CO_2 and H_2S rich magmatic hydrothermal gases could have dissolved into the fluid. As a consequence, H_2S gas would be oxidized into H_2SO_4, a process that can increase the sulfate concertation and alter the original meteoric water from generally oxic and slightly alkaline to reduced and acidic (Vigni et al., 2022).

Overall, T1 and T2 ores in the ZID display strong actinolization. This can be observed through the replacement of primary minerals like quartz and biotite, and also a strong trend in the quartz bands of T1 ore being replaced by ferro actinolite bands (Fig. 13A, C, E). This wall rock alteration and mineral replacement in the ZID indicates that the initial high-grade ore forming fluid was characterized by reducing, acidic conditions. For example, the replacement of biotite in the original IF with ferro actinolite (Fig. 13B) may have followed the reaction of Zhang et al. (2014), whereby:

[R1] $2KFe_3AlSi_3O_{10}(OH)_2$ (biotite) + $2Ca^{2+}$ + $2SiO_2$ ⇔

$Ca_2Fe_5Si_8O_{22}(OH)_2$ (ferro actinolite) + Al_2O_3 + 2 K^+ + Fe^{2+} + H_2O.

In the ZID, desilicification is mainly driven by exchange with a reducing fluid, where primary minerals such as chlorite and silica within the T1 ore and IF are replaced by ferro actinolite in the T2 ore (Fig. 13D, F):

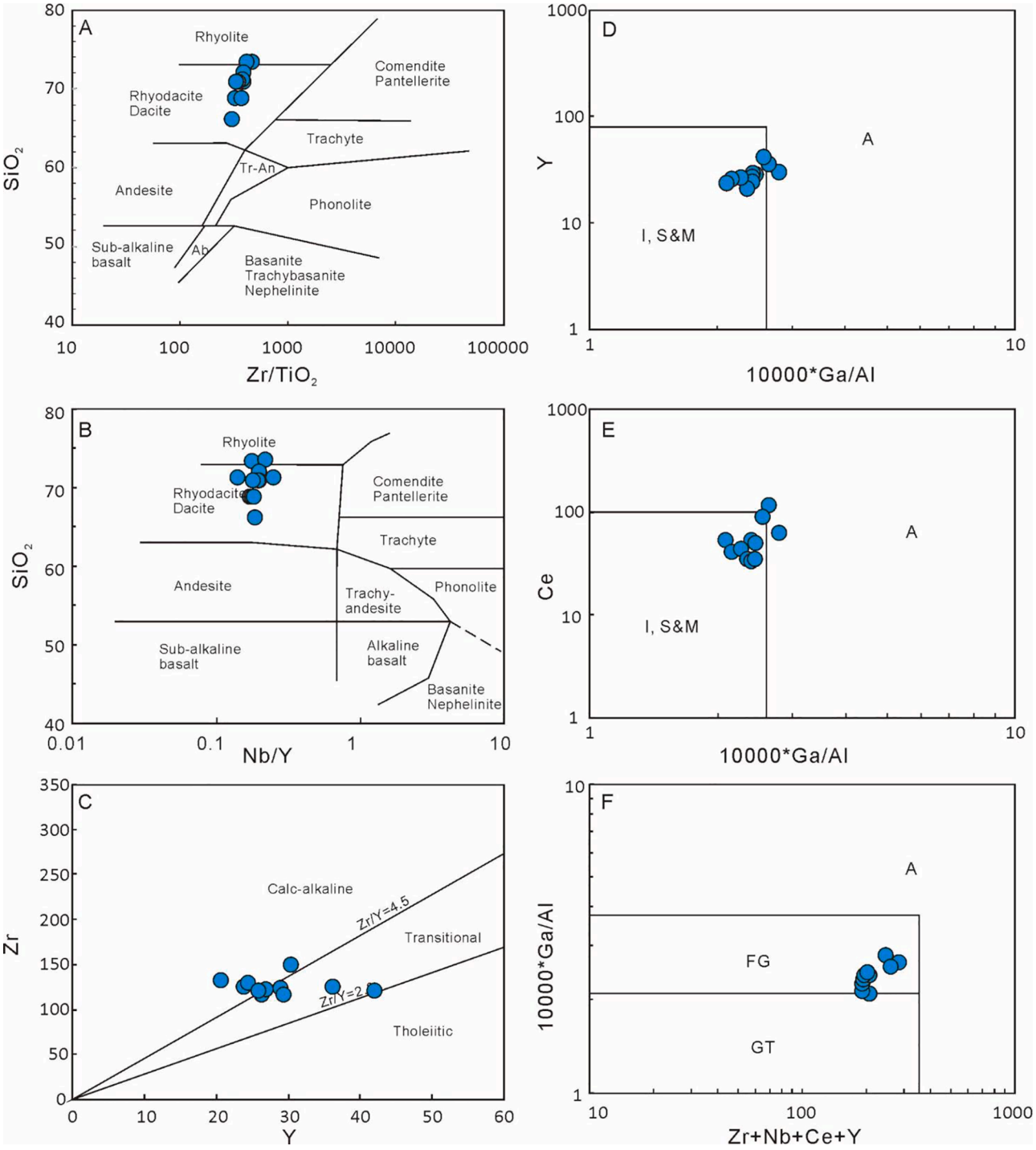

Fig. 9. Geochemical classification plots for the dacite-porphyry: (A) SiO_2 versus Zr/TiO_2; (B) SiO_2 versus Nb/Y (after Winchester and Floyd, 1977); (C) Zr versus Y (after Ross and Bédard, 2009); (D) Y vs Ga/Al cross plot; (E) Ce versus Ga/Al cross plot; and (F) Ga/Al versus Zr + Nb + Ce + Y cross plot (after Whalen et al., 1987).

[R2] $5Fe_6Si_4O_{10}(OH)_8$(chlorite) + $12CaCO_3$ (calcite) + $28SiO_2 \Leftrightarrow 6Ca_2Fe_5Si_8O_{22}(OH)_2 + 12CO_2 + 14H_2O$ (Phillips, 1986)

While the magnetite-ferro actinolite veins indicate highly acidic fluids that can dissolve Fe and Al (pH < 3, Pirajno, 2008), and subsequently transport of an iron-rich fluid through fractures. Following transport, iron recrystallization may have altered precursor magnetite grains and resulted in larger crystals enriched in iron (Zhang et al., 2014). During the later stages of the fluid alteration, temperature would have decreased to <350 °C, the observed magnetite mineralization indicates the continuous consumption of SO_4^{2-} resulted in the progressive depletion and iron-sulfide mineralization (e.g., pyrite). Such an interpretations is consistent with the sulfur isotope characteristics and wall rock alteration (e.g., veins and disseminated pyrite grains) observed in the ZID:

[*R*3] $3Fe^{2+} + SO_4^{2-} + 4OH^- \Leftrightarrow Fe_3O_4 + SO_2 + 2H_2O$

Overall, a multistage upgrading processes involving the leaching of silica and subsequent magnetite remobilization from the original sedimentary iron formations in the ZID led to the development of high-grade

Table 3
Zircon U-Pb dating results for the dacite-porphyry (sample TZK 13–1-1), Zankan iron deposit.

	$^{238}U(10^{-6})$	$^{232}Th(10^{-6})$	Th/U	$^{207}Pb/^{235}U$	±σ	$^{206}Pb/^{238}U$	±σ	$^{207}Pb/^{206}Pb$	±σ	$^{206}Pb/^{238}Pb$ (Ma)	±σ
1	2994	2302	0.77	0.64	0.029	0.08	0.0018	0.05	0.0025	514	10.8
2	2019	860	0.43	0.64	0.0363	0.09	0.0019	0.05	0.0032	529	11.5
3	2136	1095	0.51	0.64	0.0355	0.09	0.0022	0.05	0.003	527	12.9
4	3182	1508	0.47	0.61	0.044	0.08	0.002	0.05	0.0038	523	11.8
5	1648	888	0.54	0.65	0.0582	0.09	0.0023	0.05	0.0048	550	13.4
6	1449	687	0.47	0.65	0.0637	0.09	0.002	0.05	0.0052	552	11.8
7	1353	579	0.43	0.7	0.055	0.09	0.0018	0.05	0.0043	574	10.7
8	2633	1185	0.45	0.64	0.056	0.08	0.0016	0.06	0.0047	514	9.7
9	2950	1690	0.57	0.71	0.0356	0.08	0.0013	0.06	0.0033	509	8
10	2066	905	0.44	0.76	0.0344	0.09	0.0014	0.06	0.0029	555	8.6
11	1750	935	0.53	0.71	0.0426	0.09	0.0017	0.05	0.0033	580	10
12	1957	1039	0.53	0.72	0.0363	0.09	0.0016	0.06	0.003	560	9.7
13	2797	1585	0.57	0.61	0.0436	0.08	0.0022	0.05	0.0041	494	13.3
14	2458	1123	0.46	0.63	0.0345	0.08	0.0021	0.06	0.0034	475	12.5
15	1817	859	0.47	1.37	0.0674	0.16	0.004	0.06	0.0031	942	22.2

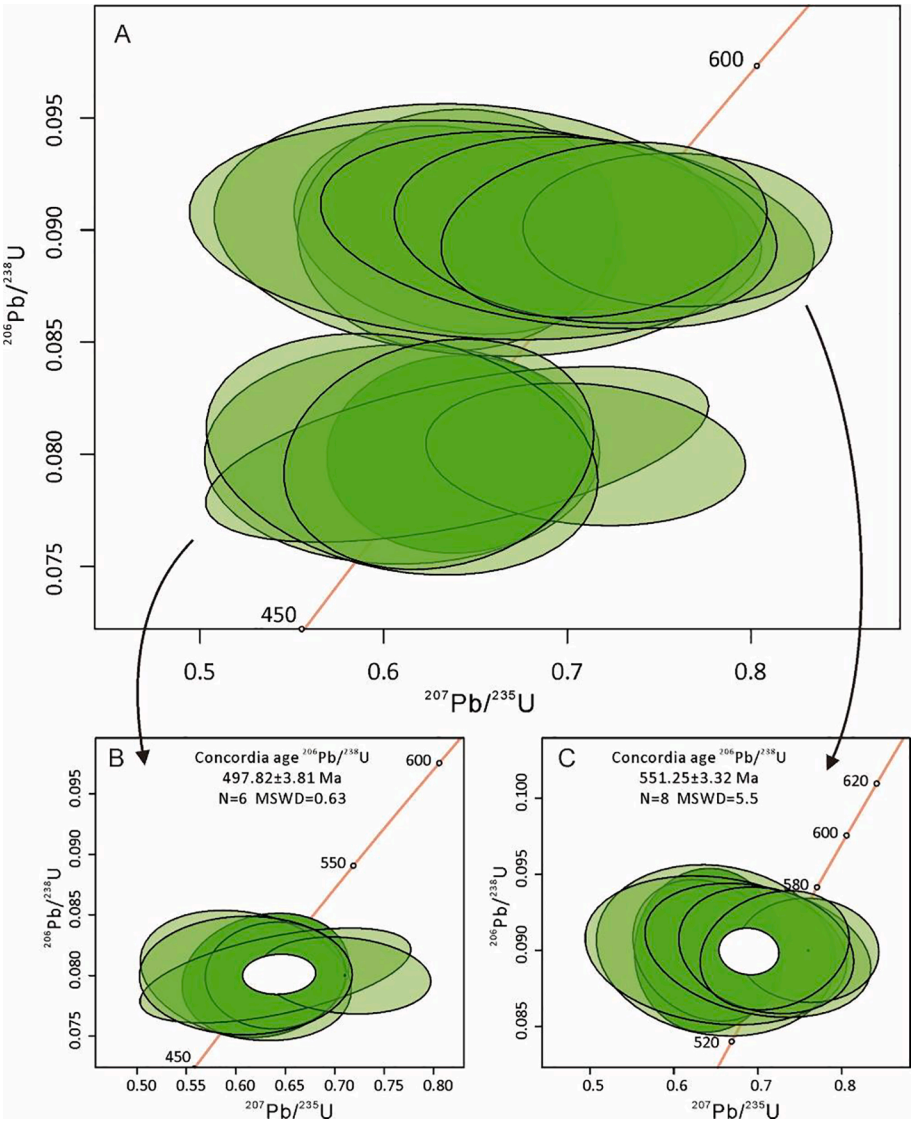

Fig.10. Concordia diagram showing LA–ICP–MS zircon U–Pb isotopic data and two calculated ages for the dacite-porphyry in the study area (A, B).

iron ores. Such processes are similar to those invoked in previously proposed hypogene-supergene models (Barley et al., 1999; Taylor et al., 2001; Thorne et al., 2004; Dalstra and Rosière, 2008; Zhang et al., 2014; Shen and Song, 2015). Based on the collective REE and isotope characteristics of the high-grade iron ores, wall rock alteration, and field observations, it is possible to propose a genetic model for the ZID high grade ores (Fig. 14):

Table 4
Hf isotopic data for zircon grains extracted from the dacite-porphyry rocks.

	T (Ma)	176Yb/177Hf	±2σ	176Lu/177Hf	±2σ	176Hf/177Hf	±2σ	176Hf/177Hf©	2sm	176Hf/177Hfi	εHf (0)	εHf (t)	2 s	TDM	TDMC	flu/Hf	TDM2
1	574	0.02582	0.00019	0.00088	0.00001	0.28230	0.00002	0.28230	2.00002	0.28229	16.8	4.5	70818.5	1346	1819	0.97	1811
2	514	0.05054	0.00064	0.00164	0.00001	0.28230	0.00003	0.28230	3.00002	0.28228	16.8	6.1	106213.3	1375	1872	0.95	1866
3	529	0.04332	0.00084	0.00163	0.00004	0.28246	0.00004	0.28246	5.00002	0.28245	11.0	0.1	177027.6	1136	1490	0.95	1484
4	527	0.05714	0.00123	0.00200	0.00005	0.28248	0.00003	0.28247	8.00002	0.28245	10.5	0.4	283242.6	1131	1472	0.94	1466
5	494	0.03800	0.00017	0.00135	0.00001	0.28235	0.00002	0.28234	11.00002	0.28233	15.2	4.7	389429.8	1297	1771	0.96	1765
6	523	0.07442	0.00086	0.00273	0.00003	0.28247	0.00006	0.28247	13.00002	0.28244	10.8	0.3	460264.7	1167	1510	0.92	1504
7	550	0.03727	0.00029	0.00135	0.00001	0.28239	0.00003	0.28239	14.00002	0.28237	13.7	2.1	495699.2	1237	1645	0.96	1638
8	552	0.03301	0.00010	0.00128	0.00000	0.28232	0.00003	0.28232	15.00002	0.28230	16.1	4.4	531108.6	1331	1795	0.96	1787
9	514	0.04429	0.00011	0.00152	0.00000	0.28247	0.00002	0.28247	16.00002	0.28245	10.7	0.1	566468.2	1123	1480	0.95	1474
10	555	0.04057	0.00042	0.00144	0.00002	0.28244	0.00002	0.28244	19.00002	0.28242	11.8	0.1	672741.9	1163	1522	0.96	1515
11	580	0.06433	0.00107	0.00245	0.00004	0.28257	0.00014	0.28257	20.00002	0.28254	−7.3	4.6	708188.6	1009	1245	0.93	1239
12	560	0.05746	0.00194	0.00199	0.00007	0.28244	0.00002	0.28244	21.00002	0.28242	11.9	0.3	743565.0	1186	1541	0.94	1534

Table 5
Oxygen isotopic composition of magnetite grains in samples from the Zankan iron deposit.

Sample name	Sample type	Mineral	$\delta^{18}O_{V\text{-}SMOW}$ (‰)
TZK11-1	High-grade Fe ore	magnetite	1.9
TZK11-2	High-grade Fe ore	magnetite	1.8
ZK80302-94	High-grade Fe ore	magnetite	2.4
ZK12-346	High-grade Fe ore	magnetite	2.7
ZK42402-86	High-grade Fe ore	magnetite	3.2
ZK42402-88	Magnetite-quartz ore	magnetite	4.4
ZK12-348	Magnetite-quartz ore	magnetite	4.6
TZK13-3-7	Magnetite-quartz ore	magnetite	4.9
TZK13-8-10	Magnetite-quartz ore	magnetite	5.1
ZK12-680	Magnetite-quartz ore	magnetite	5.2
TZK13-8-3	Magnetite-quartz ore	magnetite	5.5

Table 6
Pyrite sulfur isotope analyses from high-grade iron ore samples, Zankan Fe deposit.

Sample name	Sample type	Mineral	$\delta^{34}S$ (‰)
TZK13-8-3	High-grade Fe ore	Pyrite	19.7
TZK13-8-10	High-grade Fe ore	Pyrite	27.3
TZK13-3-7	High-grade Fe ore	Pyrite	19.1
ZK42402-88	High-grade Fe ore	Pyrite	22.7
ZK42402-86	High-grade Fe ore	Pyrite	23.2
ZKY-3*	High-grade Fe ore	Pyrite	28.2
ZK10102-ST_1*	Gypsum vein	Gypsum	35.8
ZK0701-ST_1*	Gypsum vein	Gypsum	37.5
ZK02′03-ST_1*	Gypsum vein	Gypsum	36.2
ZK10′05ST_1*	Gypsum vein	Gypsum	37.1

* Chen, 2012.

(1) Prior to 541.8 Ma, the Taxkorgan region was tectonically controlled by subduction of the Proto-Tethys Ocean beneath the TTT. This subduction provided significant hydrothermal input to the back-arc basin and resulted in the deposition of large sedimentary iron formations in the ZID.
(2) Between 541.8 and 505 Ma, a large suit of bimodal volcanics developed in the Taxkorgan area. This shift in tectonic regime, from subduction to back-arc rifting began ~ 540 Ma, given the youngest detrital zircons yield an age of 541.8 Ma in the ZID.
(3) Following this tectonic shift, at ~ 498 Ma the IFs of the ZID were intruded by the dacite-porphyry, resulting in the formation of the IF xenocrysts within the volcanics. This intrusion resulted in the development of major fracture zones proximal to the intrusion and providing conduits for hydrothermal alteration. During a late stage of intrusive event, meteoric water infiltrated the ZID and transmitted abundant SO_4^{2-} to depth along the structure zone. Heat from the magma chamber and SO_4^{2-} rich fluids led to thermochemical sulfate reduction which then generated a low pH fluid enriched in H_2S. Additionally, abundant hydrothermal H_2S gas from the magma chamber of the dacite-porphyry dissolved into the meteoric water and led to a decrease of the water pH as well. These processes promoted the leaching of silica from the IF, along with magnetite remobilization, in the high-grade iron ores hosted in the ZID.
(4) Residual magnetite carried by the high-grade ore forming fluid filled the fracture zones resulting in the magnetite-ferro actinolite veins observed.

6. Conclusions

Petrology coupled to major and trace element geochemistry and isotopic ratios provide critical insights into the deposition of the Zankan Iron Deposit (ZID) and the processes that led to the formation of high-grade iron ore deposits hosted within. When combined with results from a previous geochronology study (Li et al., 2015), this points to the

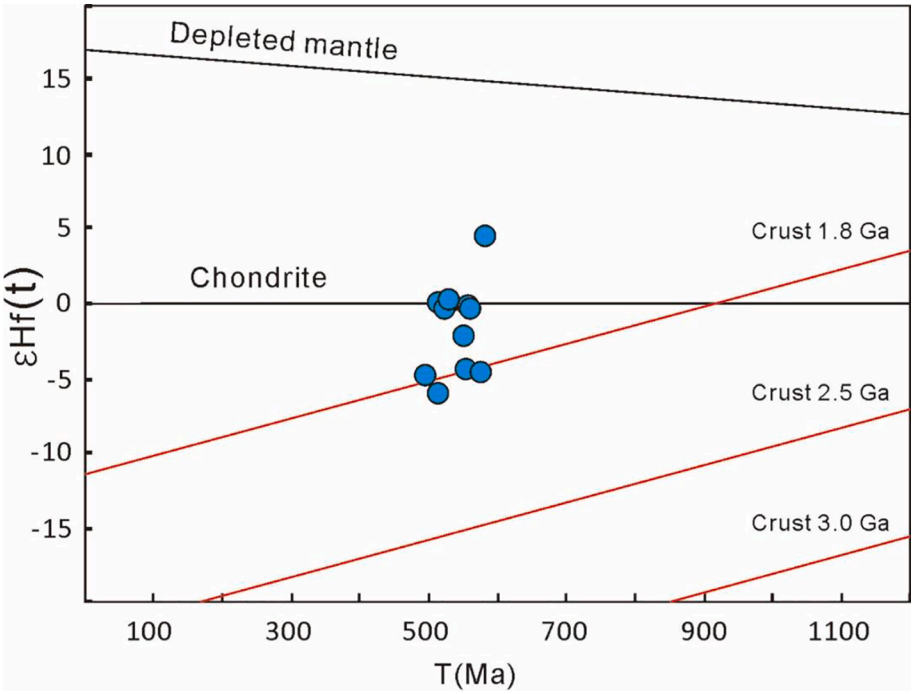

Fig. 11. Age (Ma) versus εHf(t) values for zircons from dacite-porphyry in the study area.

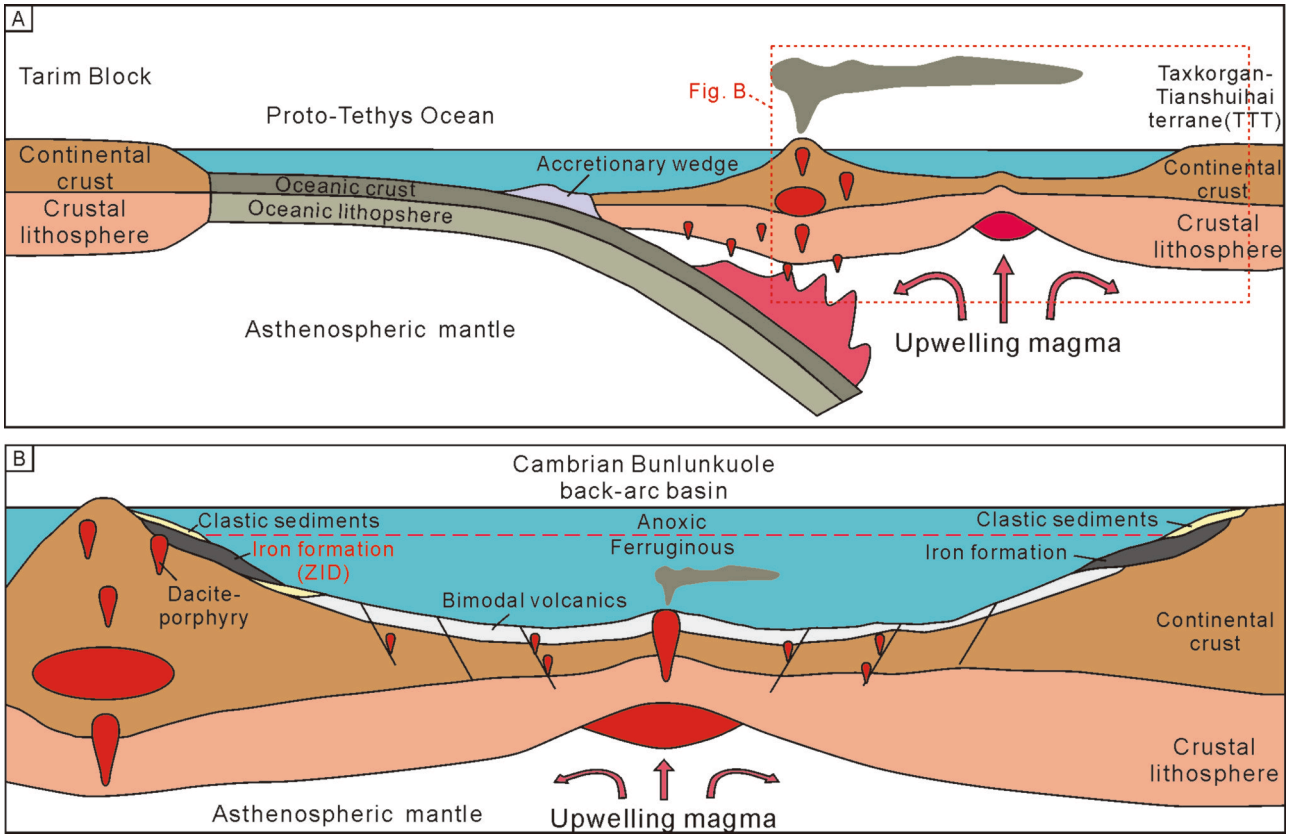

Fig. 12. Conceptual tectonic setting model for the Cambrian Bulunkuole Group, illustrating (A) the subduction of the Proto-Tethys Ocean beneath the Taxkorgan-Tianshuihai Terranes and (B) the Bunlunkuole back-arc basin (modified from Peng et al., 2021). Panel 'B' is a close-up from panel 'A'.

formation of the high-grade iron ore in the ZID occurring after 498 Ma.

Given the intimate geological relationship between the dacite-porphyry and high-grade ores in the ZID, geochemical relationships were used to constrain the tectonic setting. Trace elements ratios indicate that the dacite-porphyry is a typical I-type igneous rock. Further, Hf isotope ratios measured in zircons suggest the intrusion was sourced by a magma generated through the partial melting of Paleo-proterozoic to Mesoproterozoic crustal material. The 497.82 Ma I-type

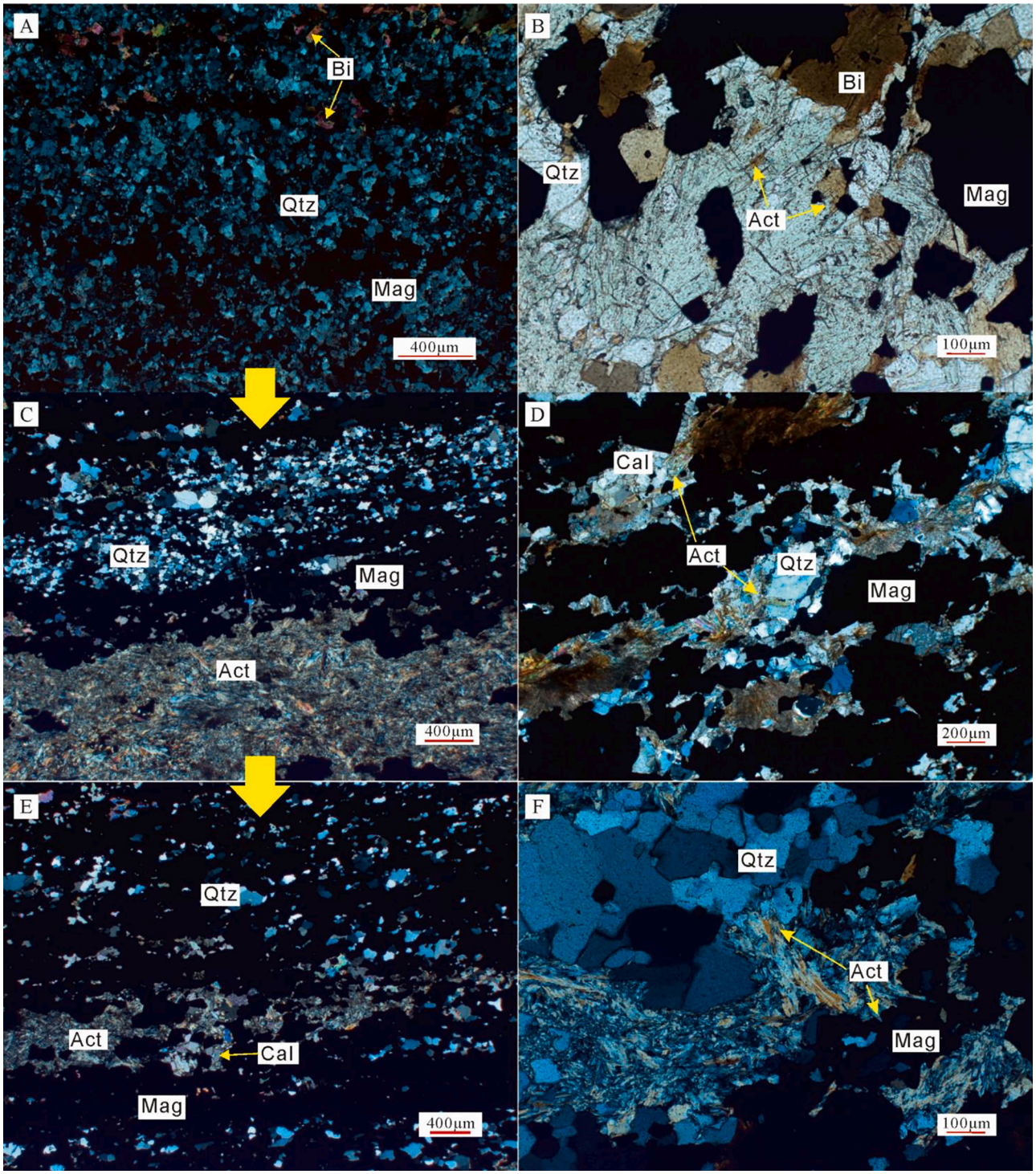

Fig. 13. Thin section photographs showing mineral replacement resulting from high-grade ore forming fluids. (A, C and E) Quartz from T1 ores is replaced by ferro actinolite, leading to the loss of initial quartz bands and enrichment of magnetite. The major mineral replacement is indicated in (E). (B) ferro actinolite replacing biotite; (D) ferro actinolite replacing calcite and quartz; and (F) ferro actinolite replace quartz and magnetite. Abbreviations: Act, ferro actinolite; Bi, biotite; Cal, calcite; Mag, magnetite; Qtz, quartz.

dacite-porphyry further suggests that back-arc rifting might have ended at this time and the region then became dominated by subduction. Increasing magma activity related to the continental arc system initiated the development of structures within the ZID, generating conduits for the subsequent circulation of the high-grade ore forming fluid.

Finally, REE patterns, along with oxygen and sulfur isotope from magnetite and pyrite grains indicate that the high-grade ores are distinct from the original iron formations, and that the ore forming fluid was primarily derived from meteoric water. Along with wall rock alteration, the high-grade iron ore forming mechanism in the ZID is attributed to the leaching of silica from the original IF, and subsequent magnetite remobilization and recrystallization. Collectively, insights gained here provide a more nuanced understanding of the processes that led to the formation of appreciable high-grade magnetite ores within the Zankan region of the Western Kunlun Mountains of northwest China.

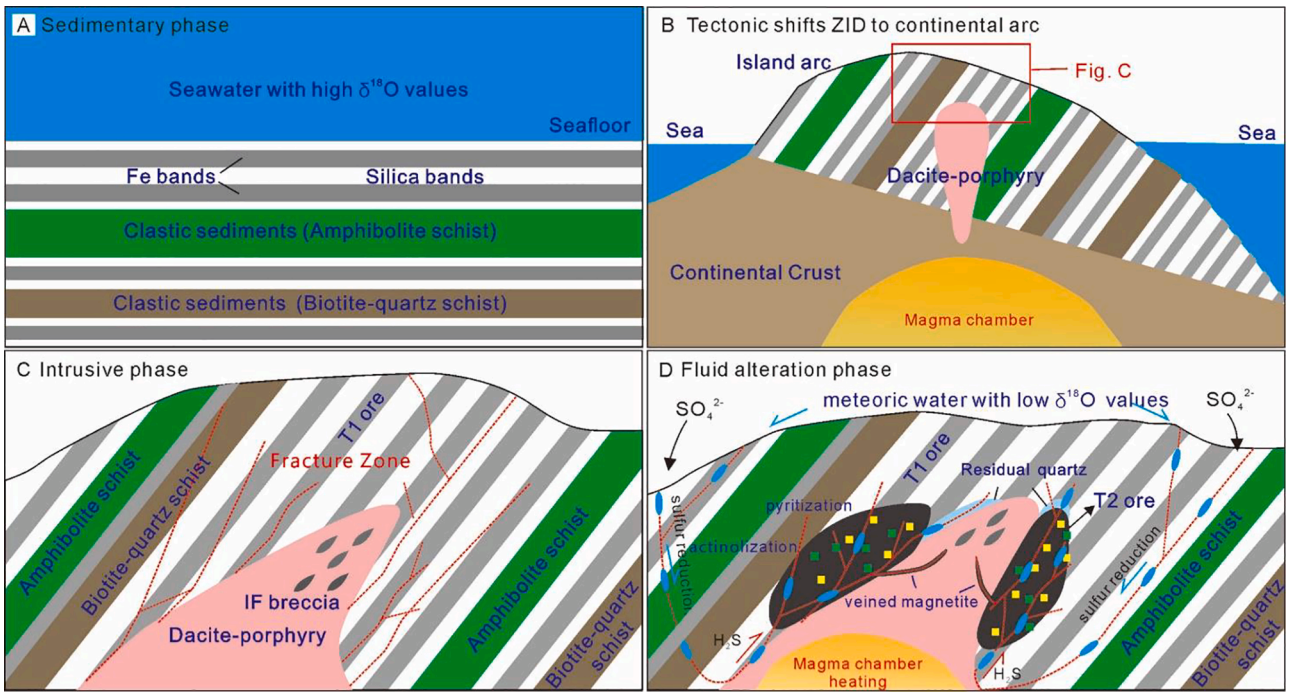

Fig. 14. Genetic model for the formation of the Zankan high-grade iron ore deposit. The sedimentary phase indicates primary chemical precipitation formed iron-rich and silica-rich bands (A). After the sedimentary phase, the tectonic activity shifts the ZID to the continental arc area (B) and further intrude by dacite-porphyry (C); for general overview of arc setting see Fig. 12. Fracture zones triggered by intrusive dacite-porphyry allows secondary ore forming fluid transport through T1 ore body (D), leading to various wall rock alteration, eventually leaching silica away and locally enriched in magnetite, thus formed T2 ores.

Declaration of Competing Interest

The authors declare that they have no known competing financial interests or personal relationships that could have appeared to influence the work reported in this paper.

Data availability

Data will be made available on request.

Acknowledgements

This research was financially supported by National Natural Science Foundation of China (Grant NO. 41372100, U1911202, U1703242, 41902205), National Key Research and Development program of China (2021YFC2900300) and Guangdong Science and Technology Department (Grant NO. GDKTP2020053500, 2020B1111370001). KOK and LJR gratefully acknowledge support from the Natural Sciences and Engineering Research Council of Canada.

Appendix A. Supplementary data

Supplementary data to this article can be found online at https://doi.org/10.1016/j.oregeorev.2022.105129.

References

Andersen, T., 2002. Correction of common lead in U-Pb analyses that do not report 204Pb. Chem. Geol. 192 (1–2), 59–79.
Barley, M.E., Pickard, A.L., Hagemann, S.G., Folkert, S.L., 1999. Hydrothermal origin for the 2 billion year old Mount Tom Price giant iron ore deposit, Hamersley Province, Western Australia. Miner. Deposita 34 (8), 784–789.
Barnes, S.J., Naldrett, A.J., Gorton, M.P., 1985. The origin of the fractionation of platinum-group elements in terrestrial magmas. Chem. Geol. 53 (3–4), 303–323.
Beukes, N.J., Mukhopadhyay, J., Gutzmer, J., 2008. Genesis of high-grade iron ores of the Archean Iron Ore Group around Noamundi, India. Econ. Geol. 103 (2), 365–386.
Blichert-Toft, J., Albarède, F., 1997. The Lu-Hf isotope geochemistry of chondrites and the evolution of the mantle-crust system. Earth Planet. Sci. Lett. 148 (1–2), 243–258.
Chappell, B.W., White, A.J.R., 1992. I-and S-type granites in the Lachlan Fold Belt. Earth Environ. Sci. Trans. Royal Soc. Edinburgh 83 (1–2), 1–26.
Chen, C.J. Study of metallogenic regularity and prospecting direction of iron deposits in Taxkorgan area, Xinjiang Province. (Master Dissertation. Wuhan, China University Geosciences, Wuhan) (2012). (in Chinese with English abstract).
Chinese National Standard: DZ/T 0200-2002, 2003. Chinese National Standard. https://www.chinesestandard.net/PDF/Sample.aspx/DZT0200-2002.
Clayton, R.N., Mayeda, T.K., 1963. The use of bromine pentafluoride in the extraction of oxygen from oxides and silicates for isotopic analysis. Geochim. Cosmochim. Acta 27 (1), 43–52.
Corfu, F., Hanchar, J.M., Hoskin, P.W., Kinny, P., 2003. Atlas of zircon textures. Rev. Mineral. Geochem. 53 (1), 469–500.
Dalstra, H.J. and Rosière, C.A., 2008. Structural controls on high-grade iron ores hosted by banded iron formation: a global perspective.
Ding, T., Tan, T., Wang, J., Zhang, C., Ye, X., Liang, J., Hao, X., Wu, B., 2021a. Field and zircon U-Pb geochronological evidence for the occurrence of Cambrian banded iron formations in the West Kunlun Orogenic Belt, China. Gondwana Res. 98, 1–16.
Ding, T., Wang, J., Tan, T., Zhang, C., Ye, X., Hao, X., 2021b. Sulfur isotopic and trace-element compositions of pyrite from the Zankan iron deposit, West Kunlun Orogenic Belt, China: Possible Early Cambrian banded iron formations. Geol. J. 56 (11), 5738–5754.
Feng, et al., 2018. Geological and Metallogenical Pattern Of The Iron Ore Belt in Taxkorgan Region. Geological Publishing House, Beijing, West Kunlun.
Findlay, D., 1994. Diagenetic boudinage, an analogue model for the control on hematite enrichment iron ores of the Hamersley Iron Province of Western Australia, and a comparison with Krivoi Rog of Ukraine, and Nimba Range, Liberia. Ore Geol. Rev. 9 (4), 311–324.
Griffin, W.L., Pearson, N.J., Belousova, E., Jackson, S.V., Van Achterbergh, E., O'Reilly, S.Y., Shee, S.R., 2000. The Hf isotope composition of cratonic mantle: LAM-MC-ICPMS analysis of zircon megacrysts in kimberlites. Geochim. Cosmochim. Acta 64 (1), 133–147.
Hagemann, S., Rosière, C., Gutzmer, J., Beukes, N.J., 2008. Banded iron formation-related high-grade iron ore. Rev. Econ. Geol.
Hu, J., Wang, H., Huang, C., Tong, L., Mu, S., Qiu, Z., 2016. Geological characteristics and age of the Dahongliutan Fe-ore deposit in the Western Kunlun orogenic belt, Xinjiang, northwestern China. J. Asian Earth Sci. 116, 1–25.
Hu, J., Huang, C., Wang, H., 2020. U-Pb zircon geochronology and geochemistry of metavolcanics and associated iron ores of the magnetite-rich BIF deposits in the Western Kunlun orogenic belt: Constraints on the depositional age, origin and tectonic setting. Ore Geol. Rev. 126, 103751.
Jiang, Y.H., Jia, R.Y., Liu, Z., Liao, S.Y., Zhao, P., Zhou, Q., 2013. Origin of Middle Triassic high-K calc-alkaline granitoids and their potassic microgranular enclaves from the western Kunlun orogen, northwest China: A record of the closure of Paleo-Tethys. Lithos 156, 13–30.

Kampschulte, A., Strauss, H., 2004. The sulfur isotopic evolution of Phanerozoic seawater based on the analysis of structurally substituted sulfate in carbonates. Chem. Geol. 204 (3–4), 255–286.
Kinny, P.D., Maas, R., 2003. Lu–Hf and Sm–Nd isotope systems in zircon. Rev. Mineral. Geochem. 53 (1), 327–341.
Konhauser, K.O., Planavsky, N.J., Hardisty, D.S., Robbins, L.J., Warchola, T.J., Haugaard, R., Lalonde, S.V., Partin, C.A., Oonk, P.B.H., Tsikos, H., Lyons, T.W., 2017. Iron formations: A global record of Neoarchaean to Palaeoproterozoic environmental history. Earth Sci. Rev. 172, 140–177.
Kusakabe, M., Mayeda, S., Nakamura, E., 1990. S, O and Sr isotope systematics of active vent materials from the Mariana backarc basin spreading axis at 18 N. Earth Planet. Sci. Lett. 100 (1–3), 275–282.
Lascelles, D.F., 2007. Black smokers and density currents: a uniformitarian model for the genesis of banded iron-formations. Ore Geol. Rev. 32 (1–2), 381–411.
Li, H.M., Yang, X.Q., Li, L.X., Zhang, Z.C., Liu, M.J., Yao, T., Chen, J., 2015. Desilicification and iron activation–reprecipitation in the high-grade magnetite ores in BIFs of the Anshan-Benxi area, China: Evidence from geology, geochemistry and stable isotopic characteristics. J. Asian Earth Sci. 113, 998–1016.
Li, Z.Q., Zhang, L.C., Xue, C.J., Zheng, M.T., Zhu, M.T., Dong, L.H., Feng, J., 2018a. Geological characteristics, formation age and high-grade ore genesis of Zankan banded iron deposit in the West Kunlun Mountains. Acta Petrol. Sinica 34 (2), 427–446.
Li, Z.Q., Zhang, L.C., Xue, C.J., Zheng, M.T., Zhu, M.T., Robbins, L.J., Slack, J.F., Planavsky, N.J., Konhauser, K.O., 2018b. Earth's youngest banded iron formation implies ferruginous conditions in the Early Cambrian ocean. Sci. Rep. 8 (1), 1–10.
Li, Z.Q., Zhang, L.C., Xue, C.J., Zhu, M.T., Zheng, M.T., Robbins, L.J., Konhauser, K.O., 2019. Genesis of the Neoproterozoic-Early Cambrian banded iron ore-bearing sedimentary rocks in the Jiertieke-Zankan iron ore belt, West Kunlun Orogenic Belt, Xinjiang (NW China). J. Asian Earth Sci. 173, 143–160.
Li, Z.Q. Genesis and depositional condition of the iron deposit belt in Taxkorgan, West Kunlun. (Doctoral Dissertation. Beijing, China University of Geosciences, Beijing) (2018). (in Chinese with English abstract).
Mattern, F., Schneider, W., 2000. Suturing of the Proto-and Paleo-Tethys oceans in the western Kunlun (Xinjiang, China). J. Asian Earth Sci. 18 (6), 637–650.
Morris, R.C., Wolff, K.H., 1985. Genesis of iron ore in banded iron-formation by supergene and supergene-metamorphic processes -a conceptual model. Handbk. Strata-bound Stratiform Ore Deposits 13, 73–235.
Pan, Y.S., Wang, Y., Matte, P., Tapponnier, P., 1994. Tectonic evolution along the geotraverse from Yecheng to Shiquanhe. Acta Geol. Sin. 68 (4), 295–307.
Peng, Z., Zheng, M., Wang, C., Zhang, L., Fan, L., Tong, X., 2021. Constraints on the age and geodynamic setting of the iron formations and anhydrite Fe-(Ba) deposits in the Bulunkuole Group of the Taxkorgan area, NW China. Ore Geol. Rev. 104121.
Phillips, G.N., 1986. Geology and alteration in the Golden Mile, Kalgoorlie. Econ. Geol. 81 (4), 779–808.
Pirajno, F., 2008. Hydrothermal Processes and Mineral Systems. Springer Science & Business Media.
Powell, C.M., Oliver, N.H., Li, Z.X., Martin, D.M., Ronaszeki, J., 1999. Synorogenic hydrothermal origin for giant Hamersley iron oxide ore bodies. Geology 27 (2), 175–178.
Pupin, J.P., 1980. Zircon and granite petrology. Contrib. Miner. Petrol. 73, 207–220.
Ramanaidou, E.R., 2009. Genesis of lateritic iron ore from banded iron-formation in the Capanema mine (Minas Gerais, Brazil). Aust. J. Earth Sci. 56 (4), 605–620.
Ross, P.S., Bédard, J.H., 2009. Magmatic affinity of modern and ancient subalkaline volcanic rocks determined from trace-element discriminant diagrams. Can. J. Earth Sci. 46 (11), 823–839.
Shen, Q.H., Song, H.X., 2015. Progress, prospecting and key scientific problems in origin researches of high-grade iron ore of the banded iron formation (BIF) in the North China Craton. Acta Petrol. Sin. 31 (10), 2795–2815.
Söderlund, U., Patchett, P.J., Vervoort, J.D., Isachsen, C.E., 2004. The 176Lu decay constant determined by Lu–Hf and U-Pb isotope systematics of Precambrian mafic intrusions. Earth Planet. Sci. Lett. 219 (3–4), 311–324.
Sun, S.S., McDonough, W.F., 1989. Chemical and isotopic systematics of oceanic basalts: implications for mantle composition and processes. Geol. Soc. London, Spec. Publicat. 42 (1), 313–345.
Taylor, D., Dalstra, H.J., Harding, A.E., Broadbent, G.C., Barley, M.E., 2001. Genesis of high-grade hematite orebodies of the Hamersley Province, Western Australia. Econ. Geol. 96 (4), 837–873.
Thorne, W.S., Hagemann, S.G., Barley, M., 2004. Petrographic and geochemical evidence for hydrothermal evolution of the North Deposit, Mt Tom Price, Western Australia. Miner. Deposita 39 (7), 766–783.
Thorne, W., Hagemann, S., Vennemann, T., Oliver, N., 2009. Oxygen isotope compositions of iron oxides from high-grade BIF-hosted iron ore deposits of the Central Hamersley Province, Western Australia: constraints on the evolution of hydrothermal fluids. Econ. Geol. 104 (7), 1019–1035.
Vermeesch, P., 2018. IsoplotR: A free and open toolbox for geochronology. Geosci. Front. 9 (5), 1479–1493.
Vigni, L.L., Daskalopoulou, K., Calabrese, S., Kyriakopoulos, K., Parello, F., Brugnone, F., D'Alessandro, W., 2022. Geochemical characterisation of the thermo-mineral waters of Greece. Environ. Geochem. Health 44 (7), 2111–2133.
Whalen, J.B., Currie, K.L., Chappell, B.W., 1987. A-type granites: geochemical characteristics, discrimination and petrogenesis. Contrib. Miner. Petrol. 95 (4), 407–419.
Winchester, J.A., Floyd, P.A., 1977. Geochemical discrimination of different magma series and their differentiation products using immobile elements. Chem. Geol. 20, 325–343.
Woodhead, J.D., Hergt, J.M., 2005. A preliminary appraisal of seven natural zircon reference materials for in situ Hf isotope determination. Geostand. Geoanal. Res. 29 (2), 183–195.
Wu, F.Y., Yang, Y.H., Xie, L.W., Yang, J.H., Xu, P., 2006. Hf isotopic compositions of the standard zircons and baddeleyites used in U-Pb geochronology. Chem. Geol. 234 (1–2), 105–126.
Xiao, W., Han, F., Windley, B.F., Yuan, C., Zhou, H., Li, J., 2003. Multiple accretionary orogenesis and episodic growth of continents: insights from the Western Kunlun Range, central Asia. Int. Geol. Rev. 45 (4), 303–328.
Xiao, W.J., Windley, B.F., Liu, D.Y., Jian, P., Liu, C.Z., Yuan, C., Sun, M., 2005. Accretionary tectonics of the Western Kunlun Orogen, China: a Paleozoic-Early Mesozoic, long-lived active continental margin with implications for the growth of Southern Eurasia. J. Geol. 113 (6), 687–705.
Yan, H., Pi, D., Jiang, S.Y., Hao, W., Cui, H., Robbins, L.J., Mänd, K., Li, L., Planavsky, N. J., Konhauser, K.O., 2020. Hydrothermally induced 34S enrichment in pyrite as an alternative explanation of the Late-Devonian sulfur isotope excursion in South China. Geochim. Cosmochim. Acta 283, 1–21.
Zhang, L.C., Feng, J., Dong, L.H., Zhu, M.T., Zheng, M.T., Li, Z.Q., Hao, Y.H., Shi, Y.J., 2016. Metallogenetic regularity of the Taxkorgan iron ore belt, West Kunlun. J. Earth Sci. Environ. 38, 427–443.
Zhang, Z.C., Hou, T., Li, H.M., Li, J.W., Zhang, Z.H., Song, X.Y., 2014. Enrichment mechanism of iron in magmatic-hydrothermal system. Acta Petrol. Sin 30 (5), 1189–1204.
Zhang, C.L., Zou, H.B., Ye, X.T., Chen, X.Y., 2018a. Tectonic evolution of the NE section of the Pamir Plateau: New evidence from field observations and zircon U-Pb geochronology. Tectonophysics 723, 27–40.
Zhang, C.L., Zou, H.B., Ye, X.T., Chen, X.Y., 2018b. Timing of subduction initiation in the Proto-Tethys Ocean: Evidence from the Cambrian gabbros from the NE Pamir Plateau. Lithos 314, 40–51.
Zhang, C.L., Zou, H.B., Ye, X.T., Chen, X.Y., 2019. Tectonic evolution of the West Kunlun Orogenic Belt along the northern margin of the Tibetan Plateau: Implications for the assembly of the Tarim terrane to Gondwana. Geosci. Front. 10 (3), 973–988.
Zheng, M.T. Ore-forming study of the Early Cambrian iron (barite) metallogenic sub-belt in the Taxkorgan iron polymetallic belt, West Kunlun. (Doctoral Dissertation. Beijing, University of Chinese Academy of Sciences) (2017). (in Chinese with English abstract).
Zheng, M.T., Wang, C.L., Zhang, L.C., Shi, Z.B., Zhu, M.T., Li, Z.Q., He, L.J., 2018. Geological and geochemical constraints on the origin of the Early Cambrian Kalaizi Fe–Ba deposit in Western Kunlun, NW China. Ore Geol. Rev. 100, 347–359.
Zhou, Y.Z., Chown, E.H., Guha, J., Lu, H.Z., 1994. Tendency and fractal pattern of migration of trace elements in source rocks during thermal event. Sci. China B 37 (6), 744–757.
Zhou, Z.J., Tang, H.S., Chen, Y.J., Chen, Z.L., 2017. Trace elements of magnetite and iron isotopes of the Zankan iron deposit, westernmost Kunlun, China: A case study of seafloor hydrothermal iron deposits. Ore Geol. Rev. 80, 1191–1205.
Zhou, Z.J., Tang, H.S., Wu, Y.S., Li, Q.G., Chen, Y.J., Chen, Z.L., 2018. Geology, geochemistry and genesis of the Zankan iron deposit in the West Kunlun Orogen, Xinjiang, China. Ore Geol. Rev. 100, 334–346.